J. Fluid Mech. (1998), *vol.* 360, *pp.* 341–374. Printed in the United Kingdom

© 1998 Cambridge University Press

Effect of axial flow on viscoelastic Taylor–Couette instability

By M. D. GRAHAM

Department of Chemical Engineering and Rheology Research Center,
University of Wisconsin-Madison, Madison, WI 53706-1691

(Received 30 January 1997 and in revised form 2 December 1997)

Viscoelastic flow instabilities can arise from gradients in elastic stresses in flows with curved streamlines. Circular Couette flow displays the prototypical instability of this type, when the azimuthal Weissenberg number We_θ is $O(\epsilon^{-1/2})$, where ϵ measures the streamline curvature. We consider here the effect of superimposed steady axial Couette or Poiseuille flow on this instability. For inertialess flow of an upper-convected Maxwell or Oldroyd-B fluid in the narrow gap limit ($\epsilon \ll 1$), the analysis predicts that the addition of a relatively weak steady axial Couette flow (axial Weissenberg number $We_z = O(1)$) can delay the onset of instability until We_θ is significantly higher than without axial flow. Weakly nonlinear analysis shows that these bifurcations are subcritical. The numerical results are consistent with a scaling analysis for $We_z \gg 1$, which shows that the critical azimuthal Weissenberg number for instability increases linearly with We_z. Non-axisymmetric disturbances are very strongly suppressed, becoming unstable only when $\epsilon^{1/2} We_\theta = O(We_z^2)$. A similar, but smaller, stabilizing effect occurs if steady axial Poiseuille flow is added. In this case, however, the bifurcations are converted from subcritical to supercritical as We_z increases. The observed stabilization is due to the axial stresses introduced by the axial flow, which overshadow the destabilizing hoop stress. If only a weak ($We_z \lesssim 1$) steady axial flow is added, the flow is actually slightly destabilized. The analysis also elucidates new aspects of the stability problems for plane shear flows, including the exact structure of the modes in the continuous spectrum, and illustrates the connection between these problems and the viscoelastic circular Couette flow.

1. Introduction

The stability and nonlinear dynamics of flow in the annular gap between concentric rotating cylinders has attracted the attention of fluid dynamicists for more than a century, because of the simplicity of the flow geometry, the rich variety of phenomena that are observed, and the relevance to technologically and scientifically important complex flows. For Newtonian flow, the analyses of Rayleigh and Taylor (see Drazin & Reid 1981) laid the groundwork for the understanding of the so-called Taylor–Couette instability of simple circular Couette flow. This instability is due to the destabilizing effect of centripetal acceleration when the inner cylinder rotates faster than the outer, and occurs when $\epsilon^{1/2} Re = O(1)$, where Re is the Reynolds number and ϵ the gap width, non-dimensionalized with cylinder radius. The square of this quantity is known as the Taylor number, Ta. Note that ϵ can be thought of as a measure of streamline curvature, scaled by gap width. The initial instability is a supercritical pitchfork bifurcation leading to a steady state consisting of axisymmetric toroidal vortices

https://doi.org/10.1017/S0022112098008611 Published online by Cambridge University Press

superimposed on the Couette flow profile. A very large number of experimental and theoretical studies have been undertaken to characterize the nonlinear dynamics and transition to turbulence in this flow (see, e.g. Swinney & Gollub 1985; Chossat & Iooss 1994). The discovery that the addition of small amounts of polymer to a Newtonian liquid could significantly reduce drag in turbulent flow led to studies of the effect of polymer additives on the Taylor–Couette instability. Experiments by a number of groups indicate that either stabilization (increase in the critical Taylor number, Ta_c) or destabilization can occur, depending on the polymer identity and concentration and the flow geometry (Rubin & Elata 1966; Denn & Roisman 1969; Giesekus 1971; Sun & Denn 1972). Early theoretical studies of the problem, using the second-order fluid model, indicate that as the first and second normal stress coefficients Ψ_1 and Ψ_2 increase, Ta_c decreases (Thomas & Walters 1964; Datta 1964; Ginn & Denn 1969; Sun & Denn 1972). Since for a polymer melt Ψ_1 is positive and Ψ_2 negative, addition of polymer has a complex effect. More recent work, using a true viscoelastic constitutive equation (Oldroyd-B) confirms the conclusion that a positive first normal stress difference has a destabilizing effect on the classical (inertially driven) Taylor–Couette instability (Avgousti & Beris 1993*b*).

In flows of concentrated polymer solutions and melts, Reynolds numbers are typically small enough for inertially driven instabilities to be absent. The seminal paper by Larson, Shaqfeh & Muller (1990, hereafter denoted LSM) showed that in circular Couette flow, instability could occur even at zero Reynolds number, due solely to viscoelastic effects. Existence of this 'viscoelastic Taylor–Couette' (VETC) instability was demonstrated experimentally and theoretically, and the basic mechanism of instability was elucidated. Instability occurs when $\epsilon^{1/2} We_\theta = O(1)$, where We_θ is the azimuthal Weissenberg number and ϵ is as defined above. This scaling reflects how large We_θ must be for hoop stress perturbations to contribute to the leading-order perturbation radial momentum balance. The instability mechanism involves the coupling of stress perturbations to the base-state velocity gradient to generate a hoop stress, which drives further perturbations. Streamline curvature is essential for instability, as inertialess viscoelastic plane Couette flow ($\epsilon = 0$) is stable at all Weissenberg numbers (Gorodtsov & Leonov 1967; Renardy 1992; Renardy & Renardy 1986). The analysis of LSM, using the upper-convected Maxwell (UCM) and Oldroyd-B constitutive models, predicts that, in contrast to the inertial case, VETC instability occurs as a Hopf bifurcation – a transition from steady to oscillatory flow. As with the inertial instability, a negative second normal stress coefficient has been shown theoretically to suppress the purely elastic instability (Beris, Avgousti & Souvaliotis 1992; Shaqfeh, Muller & Larson 1992).

Fully nonlinear calculations for axisymmetric perturbations (Northey, Armstrong & Brown 1992; Avgousti, Liu & Beris 1993; Avgousti & Beris 1993*b*) predict that (for finite ϵ) the initial bifurcation is supercritical and leads to a solution with standing wave structure in the axial direction and an approximate travelling wave structure in the radial. Linear stability calculations for non-axisymmetric flows by Sureshkumar, Beris & Avgousti (1994) and Joo & Shaqfeh (1994) predict that non-axisymmetric perturbations are in fact the most dangerous, for UCM and Oldroyd-B fluids. The most dangerous azimuthal wavenumber was observed to be typically between 1 and 3. Through an *a posteriori* energy analysis, Joo & Shaqfeh (1994) showed that the detailed mechanism for non-axisymmetric instabilities is different from that for axisymmetric ones – coupling between base-state hoop stress and non-axisymmetric radial velocity perturbations drives an increase in perturbation shear stress, which leads to increased hoop stress through coupling with the base-state

https://doi.org/10.1017/S0022112098008611 Published online by Cambridge University Press

velocity gradient. Sureshkumar *et al.* (1994) performed nonlinear simulations of the non-axisymmetric problem, showing that for sufficiently small gaps, the instability could be subcritical. When the Reynolds number is non-zero, it is possible for multiple modes to simultaneously destabilize, at so-called codimension-2 bifurcation points. Nonlinear analysis near these points is often fruitful, revealing the first effects of interaction between modes. Renardy *et al.* (1996) performed weakly nonlinear analysis near some such points for an upper-convected Maxwell fluid, finding that all of the bifurcating branches at these points are unstable.

Experiments also exhibit an oscillatory instability (LSM; Muller, Shaqfeh & Larson 1993), apparently subcritical, but a very detailed and sensitive experimental study (Baumert & Muller 1995) shows an initial instability that is actually a transition to a weak, axisymmetric, steady flow. No theoretical analysis has yet reproduced this observation.

Purely elastic instabilities due to streamline curvature have also been observed in other flows (cf. Shaqfeh 1996). Furthermore, Pakdel & McKinley (1996) have described a method for generalizing the instability criterion found by LSM to complex flow geometries such as the lid-driven cavity. The observation of related instabilities in a variety of situations suggests that elastic instabilities are ubiquitous in complex shear-dominated viscoelastic flows.

In polymer processing (e.g. adhesive coating) operations, instability is undesirable as a rule, so it is of practical importance as well as fundamental interest to explore means of suppressing flow instability. In a number of Newtonian single and multiphase flow problems, it has been observed that the imposition of relatively small steady or oscillatory secondary flows may have significant effects on stability. In many examples, instability may be suppressed to an appreciable degree by a small modification of the flow. In particular, it has been found both theoretically and experimentally that if the classical (Newtonian) Taylor–Couette problem is modified by adding a steady axial pressure-driven flow with axial Reynolds number greater than about 10, the critical Taylor number is increased substantially (Chandrasekhar 1981). Recent experimental and computational results (Weisberg, Kevrekidis & Smits 1997; Marques & Lopez 1997) show that an oscillatory shear flow can also significantly stabilize this flow.

The present work is an exploration of axial flow effects on purely elastic VETC instability. In addition to the general observation that secondary flow may be stabilizing, this study is motivated by the fact that a negative second normal stress coefficient suppresses the VETC instability, so that axial flow, which induces a negative second normal stress difference, might also be expected to lead to stabilization. Furthermore, there is a paucity of stability results for non-planar viscoelastic flow. After formulating the linear and weakly nonlinear stability problems in the narrow gap limit, we present a scaling analysis that predicts that axial flow should lead to significant stabilization. Numerical linear stability analysis confirms that this is indeed the case once the axial Weissenberg number is large enough, for both superimposed axial Couette and Poiseuille flows. Small axial shear rates, however, destabilize the flow. Weakly nonlinear analysis shows that in addition to moving the destabilizing bifurcation point, axial flow can in some cases change the criticality of the bifurcation. The basic mechanism of stabilization is elucidated: the axial tension in the fluid due to the axial shear flow leads to increased resistance of the flow to axial gradients and thus increased stability. The destabilization mechanism at small We_z is also shown, through an *a posteriori* analysis of the terms in the governing equations. Furthermore, the stability problem and resulting eigenvalue spectrum for pure circular flow are shown to be related to those for plane Couette and Poiseuille flows, reflecting an underlying unity of the

https://doi.org/10.1017/S0022112098008611 Published online by Cambridge University Press

various problems. These plane flows are the topic of Appendix A, which contains a brief overview and some new results regarding their spectra, including an exact solution for the modes corresponding to the continuous spectrum of plane Couette flow.

2. Formulation

2.1. *Geometry and governing equations*

We consider the inertialess flow of an upper-convected Maxwell or Oldroyd-B fluid in the annular region between infinitely long concentric circular cylinders. The fluid has relaxation time λ; the polymer and solvent contributions to the viscosity are η_p and η_s, respectively. The ratio η_s/η_p is denoted by S. In all cases, the inner cylinder, with radius R_1, is rotating with angular velocity Ω. The outer cylinder, with radius R_2, is stationary. The dimensionless constitutive, vorticity and continuity equations are

$$\frac{\partial \boldsymbol{\tau}}{\partial t} = \frac{1}{S+1}\left(\nabla \boldsymbol{v} + \nabla \boldsymbol{v}^T\right) - \boldsymbol{v}\cdot\nabla\boldsymbol{\tau} + \boldsymbol{\tau}\cdot\nabla\boldsymbol{v} + (\boldsymbol{\tau}\cdot\nabla\boldsymbol{v})^T - \frac{1}{We_\theta}\boldsymbol{\tau}, \tag{2.1}$$

$$0 = \nabla \times \nabla\cdot\boldsymbol{\tau} + \frac{We_\theta\, S}{S+1}\nabla\times\nabla^2\boldsymbol{v}, \tag{2.2}$$

$$0 = \nabla\cdot\boldsymbol{v}, \tag{2.3}$$

where $\boldsymbol{v}$ is velocity and $\boldsymbol{\tau}$ is the polymer stress tensor. No-slip boundary conditions are imposed at the two cylinders. The azimuthal Weissenberg number We_θ is

$$We_\theta = \frac{\lambda\Omega(1-\epsilon)}{\epsilon},$$

where

$$\epsilon = \frac{R_2 - R_1}{R_2}.$$

Note that $\epsilon/(1-\epsilon)$ measures the maximum streamline curvature. Length is scaled with the gap width $R_2 - R_1 = \epsilon R_2$, time with $\epsilon/((1-\epsilon)\Omega)$, velocity with the speed of inner cylinder rotation $(1-\epsilon)R_2\Omega$ and stress with $(\eta_s+\eta_p)/\lambda$. The dimensionless flow domain is $\{(r,\theta,z) : (1-\epsilon)/\epsilon < r < 1/\epsilon, 0 < \theta \leqslant 2\pi, -\infty < z < \infty\}$. For convenience, a new radial coordinate is defined: $\rho = r + 1 - 1/\epsilon$, so $\rho = 0$ is the inner cylinder and $\rho = 1$ the outer. We will refer to the pure circular Couette flow limit as CC.

When axial flow is present, another dimensionless group, the axial Weissenberg number, We_z, is important. If axial Couette flow is imposed, by moving the inner cylinder axially with dimensional speed V, then

$$We_z = \frac{\lambda V(1-\epsilon)}{R_2\epsilon}.$$

We denote this case by CCAC (Circular Couette with imposed Axial Couette flow). If axial Poiseuille flow is imposed, by introducing a dimensional axial pressure gradient P_z, then

$$We_z = \frac{-P_z\lambda\epsilon R_2}{2(\eta_s+\eta_p)}.$$

This definition is based on the wall shear rate, so in both the Couette and Poiseuille cases We_z measures (to within $O(\epsilon)$) the maximum shear rate. This case is denoted by CCAP (Circular Couette with imposed Axial Poiseuille flow). At leading order in ϵ, as $We_\theta \to 0$ the flow reduces to plane Couette (PC) or plane Poiseuille (PP) flow.

https://doi.org/10.1017/S0022112098008611 Published online by Cambridge University Press

Our interest is in the evolution of perturbations $\tilde{\boldsymbol{\tau}}, \tilde{\boldsymbol{v}}$ of the simple viscometric steady states nominally exhibited in this geometry. We define a vector of perturbations: $\boldsymbol{u} = (\tilde{\tau}_{rr}, \tilde{\tau}_{r\theta}, \tilde{\tau}_{rz}, \tilde{\tau}_{\theta\theta}, \tilde{\tau}_{\theta z}, \tilde{\tau}_{zz}, \tilde{v}_r, \tilde{v}_\theta, \tilde{v}_z)$, where, for example, $\tilde{\tau}_{\theta\theta} = \tau_{\theta\theta} - \bar{\tau}_{\theta\theta}$ and $\bar{\tau}_{\theta\theta}$ is the steady value of $\tau_{\theta\theta}$. (The steady states for the CCAC and CCAP flows are shown in Appendix B.) Now (2.1) can be succinctly written

$$\boldsymbol{E}\frac{\partial \boldsymbol{u}}{\partial t} = \boldsymbol{L}\boldsymbol{u} + \boldsymbol{N}(\boldsymbol{u}), \tag{2.4}$$

where $\boldsymbol{L}\boldsymbol{u}$ is the linearization of the right-hand side of (2.1) about the steady-state flow and $\boldsymbol{N}(\boldsymbol{u})$ is the strictly nonlinear term $-\tilde{\boldsymbol{v}}\cdot\nabla\tilde{\boldsymbol{\tau}} + \tilde{\boldsymbol{\tau}}\cdot\nabla\tilde{\boldsymbol{v}} + (\tilde{\boldsymbol{\tau}}\cdot\nabla\tilde{\boldsymbol{v}})^T$. The matrix $\boldsymbol{E}$ is diagonal, with ones on the first six diagonals and zeros elsewhere.

Considering the constitutive equations when $We_\theta \gg 1$ shows that the perturbation stresses must scale with We_θ in the same way that the steady-state stresses do, for a balance of terms to be maintained. This fact has an important implication for the dominant balances in the momentum equations. Consider the θ-component of the vorticity equation (assuming for the moment axisymmetry and zero solvent viscosity):

$$\frac{\partial^2\tilde{\tau}_{rr}}{\partial r\,\partial z} + \frac{\partial^2\tilde{\tau}_{rz}}{\partial z^2} - \frac{\partial^2\tilde{\tau}_{rz}}{\partial r^2} - \frac{1}{r}\frac{\partial\tilde{\tau}_{\theta\theta}}{\partial z} - \frac{\partial^2\tilde{\tau}_{zz}}{\partial r\,\partial z} = 0.$$

Assuming $O(1)$ gradients, all terms except the fourth are $O(1)$; this term, representing the contribution of $\tilde{\tau}_{\theta\theta}$ to the r-momentum balance – the effect of curvature – is $O(\epsilon We_\theta^2)$. For this term to remain in the leading-order balance, We_θ must therefore scale as $O(\epsilon^{-1/2})$ as $\epsilon \to 0$. If it does not, the problem reduces to one of plane shear flow, which is always stable. This scaling was first recognized by LSM; we enforce it by defining a new scaled Weissenberg number $Wp = \epsilon^{1/2}We_\theta$, which is $O(1)$ as $\epsilon \to 0$. Correspondingly, the following scalings are enforced: $\tilde{\tau}_{rr} = O(1), \tilde{\tau}_{r\theta} = O(\epsilon^{-1/2}), \tilde{\tau}_{rz} = O(1), \tilde{\tau}_{\theta\theta} = O(\epsilon^{-1}), \tilde{\tau}_{\theta z} = O(\epsilon^{-1/2}), \tilde{\tau}_{zz} = O(1), \tilde{v}_r = O(\epsilon^{1/2}), \tilde{v}_\theta = O(1), \tilde{v}_z = O(\epsilon^{1/2})$. Finally, a factor of $\epsilon^{1/2}$ is absorbed into the time, giving a dimensionless time scaled on the polymer relaxation time. These scalings were used implicitly in the work of LSM, and are imposed in the remainder of the present analysis.

In this paper we consider exclusively the leading-order behaviour in the narrow gap limit $\epsilon \to 0$. In this limit, the steady-state stresses and velocity gradients are those for plane shear flow. No curvature terms appear in the constitutive equations; the only effect of curvature is the presence of $\tilde{\tau}_{\theta\theta}$ in the r-momentum balance when $Wp = O(1)$.

2.2. *Linear stability analysis*

For the most part, this work is concerned with the linear stability of the steady-state flow. Letting $\boldsymbol{u} = \delta\boldsymbol{u}_1 + O(\delta^2)$, where $\delta \ll 1$ is the amplitude of the perturbation, the leading-order problem is just the linear stability problem

$$\boldsymbol{E}\frac{\partial \boldsymbol{u}_1}{\partial t} = \boldsymbol{L}\boldsymbol{u}_1. \tag{2.5}$$

We consider only axially periodic perturbations, which have the form

$$\boldsymbol{u}_1(\rho,\theta,z,t) = \boldsymbol{\xi}(\rho)\mathrm{e}^{\mathrm{i}\alpha(z-ct)+\mathrm{i}n\theta} + \text{c.c.},$$

where $\boldsymbol{\xi} = (\hat{\tau}_{rr}(\rho), \hat{\tau}_{r\theta}(\rho), \hat{\tau}_{rz}(\rho), \hat{\tau}_{\theta\theta}(\rho), \hat{\tau}_{\theta z}(\rho), \hat{\tau}_{zz}(\rho), \hat{v}_r(\rho), \hat{v}_\theta(\rho), \hat{v}_z(\rho))$ contains the radial structure of the perturbation. Here $\alpha \in \mathbb{R}$ is the axial wavenumber of the perturbations and $n \in \mathbb{Z}$ the azimuthal wavenumber. The wave speed is given by c, which is $O(1)$. Given Wp, We_z, S, α and n, we now have a generalized eigenvalue problem, with

https://doi.org/10.1017/S0022112098008611 Published online by Cambridge University Press

eigenvalue c. If the imaginary part of c, denoted c_i, is positive, the steady state is unstable. The real part of c is denoted c_r and determines the rate of axial propagation of perturbations, the wave speed.

As mentioned in the introduction, finite-gap calculations of the pure CC problem predict that non-axisymmetric ($n \neq 0$) perturbations are generally the most destabilizing. Joo & Shaqfeh (1994) note that, in the pure CC case, when n is $O(1)$, it does not appear in the leading-order (in ϵ) stability problem. This also holds true in the presence of axial flow and in the full nonlinear problem. Therefore, all modes with $n = O(1)$ have the same bifurcation characteristics at leading order as do axisymmetric modes. Joo & Shaqfeh included non-axisymmetric effects by keeping terms of order $\epsilon^{1/2}$ in their calculations. We construct an equivalent formulation by considering azimuthal wavenumbers of $O(\epsilon^{-1/2})$: we let $n = \tilde{n}\epsilon^{-1/2}$, where $\tilde{n} = O(1)$, and keep leading-order terms. Now the effects of non-axisymmetry can be considered without the complication of finite-gap effects. With this scaling, the terms from the upper-convected derivative that contain θ-derivatives are now present, but the terms from the rate of deformation are absent. The eigenvalue problem is

$$\mathrm{i}\alpha c \boldsymbol{E}\boldsymbol{\xi} = \boldsymbol{L}_{\alpha,\tilde{n}}\boldsymbol{\xi}. \tag{2.6}$$

The operator $\boldsymbol{L}_{\alpha,\tilde{n}}$ is given in Appendix B.

It is also of interest to consider the stability of modes with $n = O(\epsilon^{-1})$: i.e. modes that vary azimuthally on the same scale as they vary radially and axially. Modes with such a fine azimuthal structure have neither been observed experimentally nor predicted theoretically, and a simple scaling argument reveals why. Taking $n = O(\epsilon^{-1})$ and requiring that We_θ be large enough for $\tilde{\tau}_{\theta\theta}$ to remain in the leading-order radial momentum balance yields that $\epsilon We_\theta^2 = O(\epsilon^{-1})$. Therefore, We_θ must be $O(\epsilon^{-1})$, rather than $O(\epsilon^{-1/2})$, for the destabilizing effect of $\tilde{\tau}_{\theta\theta}$ to play a role. Because of this result, and corroborating simulations, this case will not be considered further.

In the absence of axial flow, the basic CC flow profile is highly symmetric. Because of this high degree of symmetry, the perturbation equations are O(2) (i.e. translation and reflection) invariant in the axial coordinate. In particular, if $g(\rho, \theta, z, t)$ is a solution, then so are both $g(\rho, \theta, -z, t)$, and $g(\rho, \theta, z - z_0, t)$, for any real z_0. Hopf bifurcations that break O(2) symmetry are always degenerate: travelling waves with equal and opposite wave speeds in the z-direction bifurcate simultaneously, and only a nonlinear analysis can determine whether the actual bifurcating solution is a travelling wave or a standing wave (equal superposition of the two travelling waves) (Golubitsky, Schaeffer & Stewart 1985). Avgousti & Beris (1993*b*) provide a detailed discussion of symmetry issues in the context of axisymmetric instabilities of CC flow. If axial flow is imposed, the reflection symmetry is lost (the O(2) symmetry is broken to SO(2)), the Hopf bifurcation is no longer degenerate, and the linear analysis determines the form of the bifurcating solution. Hopf bifurcations in SO(2) symmetric systems, i.e. when $We_z \neq 0$, take the form of non-degenerate travelling waves (Iooss & Joseph 1990).

2.3. *Numerical analysis of the linear stability problem*

The differential eigenvalue problem described above and detailed in Appendix B is discretized with a Chebyshev collocation technique (Canuto *et al.* 1988) using $N + 1$ collocation points. The number of points used for a particular calculation is indicated in the figure caption for that calculation. We typically use $N = 64$; $N = 32$ suffices for calculations at $We_z = 0$, but $N = 128$ is required for calculations at large We_z and small Wp. Continuity is used to eliminate $\hat{v}_z$. The boundary conditions on $\hat{v}_r$ are

https://doi.org/10.1017/S0022112098008611 Published online by Cambridge University Press

imposed by substituting them for the θ-vorticity equation at the boundary collocation points and the first point in from either boundary. This is standard when more than one boundary condition must be satisfied at a boundary (Canuto *et al.* 1988). Similarly, the boundary condition on $\hat{v}_\theta$ is imposed by substituting it for the r-vorticity equation at each boundary. The resulting algebraic generalized eigenvalue problem is solved with a public-domain subroutine that uses QZ factorization (Garbow 1978). Since $\boldsymbol{E}$ is singular, there are many 'infinite' eigenvalues, which numerically have moduli greater than 10^8. These are discarded.

The presence of spurious eigenvalues is well-documented in the stability analysis for PP and PC flows (Ho & Denn 1977; Renardy & Renardy 1986; Keiller 1992), so we expect that such eigenvalues might arise in the present analysis when $We_z \neq 0$. These eigenvalues are grid dependent and may lead to artificial instabilities. In the formulation used here, where pressure is eliminated by using the vorticity equation, four spurious eigenvalues appear in the axisymmetric problem; in the Poiseuille case all have real parts less than zero and in the Couette case two eigenvalues have negative real parts and the others have real parts greater than the axial velocity of the inner cylinder. Thus, in both cases, the spurious eigenvalues correspond to wave speeds outside the range of fluid velocities of the steady-state motion. Ho & Denn (1977) and Renardy & Renardy (1986) using similar formulations for the pure PP and PC problems, observe similar results. In the primitive variable formulation used by Sureshkumar & Beris (1995*b*), spurious modes of this type are absent, so their origin apparently lies in our treatment of pressure. In fact, after the completion of the computations shown in this paper, the present author, in collaboration with V. V. Ramanan, found that a primitive variable formulation with a staggered collocation point grid for pressure displays no spurious modes, consistent with the results of Sureshkumar & Beris (1995*b*). Nevertheless, with the present formulation, the spurious modes can be eliminated from the axisymmetric problem by simply imposing (numerical) Neumann boundary conditions on some of the stresses (i.e. by replacing the equation for the stress at the boundary collocation points with the discretized Neumann condition). This 'boundary regularization', applied just to $\hat{\tau}_{rr}, \hat{\tau}_{rz}$ and $\hat{\tau}_{zz}$, removes the spurious eigenvalues, leaving the true eigenvalues essentially unchanged. This has been checked with pure PC flow, where the spectrum is known exactly, as well as with randomly chosen CC runs, with and without axial flow. Figure 16 shows a calculation of the PC spectrum with and without boundary regularization. For the non-axisymmetric problem, spurious modes are still present (in the pressure-free formulation) after boundary regularization, but remained sufficiently stable that they only became important at Wp values far above the minimum critical value for instability.

Even after elimination of these spurious modes, artificial instability can occur if both Wp and We_z are non-zero. This instability arises because some of the poorly resolved components of the continuous spectrum (see Appendix A) cross the real axis. (This never occurs if $Wp = 0$.) This problem can be alleviated by regularizing the constitutive equation with a diffusive term $D_s\nabla^2\boldsymbol{\tau}$ (cf. Sureshkumar & Beris 1995*a*). However, this regularization does influence the true eigenvalues (unlike the boundary regularization), so for all results presented here, only boundary regularization was imposed, and results were checked to verify that no artificial instability was present.

The codes used here were validated by comparisons with several sources. Pure CC flow was checked with results of LSM, as well as an asymptotic lower bound derived below. The PC flow limit was checked against the exact analytical results of Gorodtsov & Leonov (1967), and the PP limit was checked against the Chebyshev

https://doi.org/10.1017/S0022112098008611 Published online by Cambridge University Press

collocation results of Sureshkumar & Beris (1995*b*) and by checking the approach of the boundary-localized modes to the Gorodtsov–Leonov modes at large α.

2.4. *Nonlinear analysis*

Once a bifurcation point Wp_c has been detected via linear stability analysis for given We_z, S, α, and $\tilde{n}$, we determine the criticality of the bifurcation through a weakly nonlinear analysis. All bifurcations considered here are Hopf bifurcations, and we use the perturbation method detailed by Iooss & Joseph (1990) to explicitly construct time-periodic solutions, with amplitude δ and frequency ω, near the bifurcation point. Only solutions with spatial period $2\pi/\alpha$ will be considered here, so sideband instabilities are not addressed. Because it will be seen that for $We_z \gtrsim 1$ axisymmetric modes are most dangerous, our nonlinear analysis will be restricted to this case. Letting $\mu = Wp - Wp_c$, $\omega_0 = -\alpha c_r$, where c_r is the wave speed at Wp_c, and $s = \omega t$, we seek a solution of the form

$$\begin{pmatrix} \boldsymbol{u}(z,s,\delta) \\ \mu(\delta) \\ \omega(\delta)-\omega_0 \end{pmatrix} = \sum_{k=1}^{\infty} \frac{\delta^k}{k!} \begin{pmatrix} \boldsymbol{u}_k(z,s) \\ \mu_k \\ \omega_k \end{pmatrix}, \tag{2.7}$$

where $\boldsymbol{u}$ is taken to contain the solution values at the Chebyshev collocation points, and is periodic in z with period $2\pi/\alpha$ and in s with period 2π. It can be shown that $\mu_k = \omega_k = 0$ for odd values of k. The goal of the present analysis is to determine μ_2, whose sign determines the criticality of the bifurcations: neglecting terms beyond $O(\delta^3)$,

$$\delta = \left(\frac{2(Wp - Wp_c)}{\mu_2} \right)^{1/2}. \tag{2.8}$$

If $\mu_2 > 0$, the bifurcation is supercritical – a finite-amplitude solution exists when $Wp > Wp_c$. A negative value of μ_2 indicates subcritical bifurcation.

The original nonlinear problem (2.4) can be rewritten

$$\omega \boldsymbol{E} \frac{\mathrm{d}\boldsymbol{u}}{\mathrm{d}s} = \boldsymbol{L}(\mu)\boldsymbol{u} + \boldsymbol{N}(\boldsymbol{u}). \tag{2.9}$$

The gradient operators in the nonlinear term take on their Cartesian representations in the narrow gap limit. The time-periodic solution is constructed order by order in δ and a solvability condition at third order gives expressions for μ_2 and ω_2. We will use the inner products

$$\langle a(z,s), b(z,s) \rangle \equiv \frac{\alpha}{4\pi^2} \int_0^{2\pi/\alpha} \int_0^{2\pi} a(z,s)\bar{b}(z,s)\, \mathrm{d}s\, \mathrm{d}z$$

and

$$[\boldsymbol{a}(z,s), \boldsymbol{b}(z,s)] \equiv \sum_{l=0}^{9(N+1)-1} \langle a_l(z,s), b_l(z,s) \rangle.$$

For the moment, the overbar denotes a complex conjugate. Also, $\langle \boldsymbol{a}(z,s), \boldsymbol{b}(z,s) \rangle$ is the vector whose lth component $\langle \boldsymbol{a}(z,s), \boldsymbol{b}(z,s) \rangle_l$ is given by $\langle a_l(z,s), b_l(z,s) \rangle$.

Applying the expansion (2.7), and considering the problem at $O(\delta^1)$, gives the linear stability problem, which we rewrite

$$\left(-\omega_0 \boldsymbol{E} \frac{\mathrm{d}}{\mathrm{d}s} + \boldsymbol{L}(0) \right) \boldsymbol{u}_1 \equiv J_0 \boldsymbol{u}_1 = 0. \tag{2.10}$$

https://doi.org/10.1017/S0022112098008611 Published online by Cambridge University Press

This problem has a non-trivial real travelling wave solution $\boldsymbol{u}_1 = \boldsymbol{z} + \bar{\boldsymbol{z}}$, where $\boldsymbol{z} = \mathrm{e}^{\mathrm{i}s}\boldsymbol{\zeta}$ and $\boldsymbol{\zeta} = \mathrm{e}^{\mathrm{i}\alpha z}\boldsymbol{\xi}$. The vector $\boldsymbol{z}^*$ is the solution to the adjoint problem $J_0^* \boldsymbol{z}^* = 0$. Now we let $\boldsymbol{A}_\alpha = -\mathrm{i}\omega_0 \boldsymbol{E} + \boldsymbol{L}_\alpha$, where $\boldsymbol{L}_\alpha$ is $\boldsymbol{L}(0)$ with $\partial/\partial z$ replaced by $\mathrm{i}\alpha$. Its components are given in Appendix B. Equation (2.10) becomes $\boldsymbol{A}_\alpha \boldsymbol{\xi} = 0$, with adjoint problem $\boldsymbol{A}_\alpha^* \boldsymbol{\xi}^* = 0$. Given Wp_c and c_r, $\boldsymbol{\xi}$ and $\boldsymbol{\xi}^*$ are simply the right and left eigenvectors of $\boldsymbol{A}_\alpha$, which we normalize so that $[\boldsymbol{\zeta}, \boldsymbol{\zeta}^*] = 1$. Now we define the amplitude δ of the solution to be

$$\delta = [\boldsymbol{u}, \boldsymbol{z}^*],$$

and require that

$$[\boldsymbol{u}_1, \boldsymbol{z}^*] - 1 = [\boldsymbol{u}_k, \boldsymbol{z}^*] = 0, \qquad k \geqslant 2. \tag{2.11}$$

It can be shown in general that $\omega_1 = \mu_1 = 0$, so the problem at $O(\delta^2)$ is

$$J_0 \boldsymbol{u}_2 = -2\boldsymbol{N}_2(\boldsymbol{u}), \tag{2.12}$$

where $\boldsymbol{N}_k(\boldsymbol{u})$ is the $O(\delta^k)$ part of $\boldsymbol{N}(\boldsymbol{u})$. The particular solution has the form

$$\boldsymbol{u}_2 = \boldsymbol{u}_{20} + \boldsymbol{u}_{22}\mathrm{e}^{2\mathrm{i}(\alpha z + s)} + \bar{\boldsymbol{u}}_{22}\mathrm{e}^{-2\mathrm{i}(\alpha z + s)}, \tag{2.13}$$

where $\boldsymbol{u}_{20}$ and $\boldsymbol{u}_{22}$ satisfy

$$\boldsymbol{L}_0 \boldsymbol{u}_{20} = -2\langle \boldsymbol{N}_2(\boldsymbol{u}), \boldsymbol{1} \rangle \tag{2.14}$$

and

$$(-2\mathrm{i}\omega_0 \boldsymbol{E} + \boldsymbol{L}_{2\alpha})\, \boldsymbol{u}_{22} = -2\langle \boldsymbol{N}_2(\boldsymbol{u}), \boldsymbol{1}\mathrm{e}^{2\mathrm{i}(\alpha z + s)} \rangle. \tag{2.15}$$

Here $\boldsymbol{1} = (1, 1, 1, \ldots)$. The first of these two equations is singular even in the exact case (i.e. without discretization). The singularity can be traced to the elimination of pressure and the null vector corresponds to simple axial Poiseuille flow. The null vector is excluded from the final solution because it corresponds to a pressure field that is not spatially periodic. Therefore, we take $\boldsymbol{u}_{20}$ to be the minimum norm solution to (2.14), which we determine by singular value decomposition. Equation (2.15) is not singular and its solution is found by LU decomposition.

At third order, the orthogonality requirement (2.11) leads to a solvability condition, whose real and imaginary parts require that

$$\mu_2 = -2\left(\frac{\mathrm{d}\alpha c_i}{\mathrm{d}\mu}\right)^{-1} \mathrm{Re}\left\{\frac{[\boldsymbol{N}_3(\boldsymbol{u}), \boldsymbol{z}^*]}{[\boldsymbol{E}\boldsymbol{u}_1, \boldsymbol{z}^*]}\right\}, \tag{2.16}$$

$$\omega_2 = -2\alpha\mu_2 \frac{\mathrm{d}c_r}{\mathrm{d}\mu} + 2\,\mathrm{Im}\left\{\frac{[\boldsymbol{N}_3(\boldsymbol{u}), \boldsymbol{z}^*]}{[\boldsymbol{E}\boldsymbol{u}_1, \boldsymbol{z}^*]}\right\}. \tag{2.17}$$

The derivatives in these expressions are evaluated at $\mu = 0$. Given the solutions $\boldsymbol{u}_1$ and $\boldsymbol{u}_2$, these formulas can be evaluated to determine the criticality of the bifurcation, from the sign of μ_2, as well as whether the oscillation frequency increases ($\omega_2 > 0$) or decreases with amplitude.

3. Results and discussion

3.1. *Instability in the absence of axial flow*

To provide a basis for the main results of this work, we begin by reviewing the pure 'viscoelastic Taylor–Couette' instability, i.e. the instability in the CC case, focusing on axisymmetric disturbances of the upper-convected Maxwell fluid. For the most part, the results reproduce those obtained by LSM. Effects of solvent viscosity and

https://doi.org/10.1017/S0022112098008611 Published online by Cambridge University Press

non-axisymmetric perturbations will be discussed in the context of the CCAC and CCAP flows.

In general, the linear stability problem must be solved numerically, as detailed above. Nevertheless, an illustrative asymptotic result can be found for short-wavelength axisymmetric disturbances. LSM showed that when $\alpha \gg 1$, Wp must be $O(\alpha^{1/2})$ for $\hat{\tau}_{\theta\theta}$ to remain in the leading-order r-momentum balance. The linearized equations governing disturbances can be reduced to a single fourth-order boundary value problem for the radial velocity $\hat{v}_r$ (LSM). Letting $S = 0, \tilde{n} = 0, R = \rho\alpha, Wp = O(\alpha^{1/2}), \hat{v}_\theta = O(Wp), c = O(\alpha^{-3/2})$, this equation is

$$\hat{v}_R'''' - 2\hat{v}_R'' + \Lambda\hat{v}_R' + \hat{v}_R = 0, \tag{3.1}$$

with boundary conditions

$$\hat{v}_R(0) = \hat{v}_R'(0) = \hat{v}_R(\alpha) = \hat{v}_R'(\alpha) = 0,$$

where

$$\Lambda = \frac{2Wp^2}{\alpha(\mathrm{i} + \alpha c Wp)^2} = O(1).$$

Here $\hat{v}_R$ is the radial velocity expressed in the scaled variable R and primes denote derivatives with respect to R. By expressing solutions as $\exp(\sigma R)$, a quartic equation in σ is found. If Λ is not purely imaginary, there are no non-trivial solutions that satisfy the boundary conditions (LSM). LSM found an approximate numerical solution, moving the boundary conditions at $R = \alpha$ to $R = \infty$, finding that instability occurs at $Wp_c \approx 1.960\alpha^{1/2}$. Numerical results of LSM and the present work, for the problem with the exact boundary condition, indicate that this formula consistently overpredicts Wp_c. Further analysis is able to provide a more precise approximation. Examination of the roots of the quartic for imaginary Λ shows that an eigenfunction that remains bounded as $\alpha \to \infty$ can only exist if $|\Lambda| \geqslant 3.0795$. Using the definition of Λ and setting $c_i = 0$, we find that as $\alpha \to \infty$, the neutral curve when $We_z = 0$ is bounded from below by the curve $Wp = 1.755\alpha^{1/2}$. This lower bound agrees very closely with the numerical results presented below. The corresponding eigenfunction is a superposition of two sinusoidal functions with different wavenumbers, which at $\Lambda = \mathrm{i}3.0795$ are 0.584α and 0.571α. Thus, in the limit $\alpha \to \infty$, the exact disturbance structure is a sum of two radially travelling waves, consistent with the numerical observations at finite α. At any finite wavenumber, there will be a slight deviation from purely sinusoidal behaviour in boundary layers of thickness α^{-1} at each wall.

The numerically determined neutral curve for $S = 0, \tilde{n} = 0, We_z = 0$ is shown in figure 1. The minimum occurs at $Wp_{c,min} = 5.93, \alpha = 6.7$. These results are in agreement with the calculations of LSM. This figure also shows the asymptotic lower bound, $Wp = 1.755\alpha^{1/2}$, derived above. Figure 2 shows the spectrum of eigenvalues at $Wp = Wp_{c,min} = 5.93, \alpha = \alpha_{min} = 6.7$ (cf. Shaqfeh *et al.* 1992). Note the pair of eigenvalues with zero imaginary part, but with opposite real part, corresponding to waves travelling in opposite directions. Nonlinear analyses for finite gaps (Northey *et al.* 1992; Avgousti *et al.* 1993; Avgousti & Beris 1993*b*) have shown that the two travelling waves have equal amplitude, so the result is a standing wave in the axial direction. A snapshot of the destabilizing disturbance, assuming standing wave structure, is shown in figure 3. Fluctuations travel radially, consistent with the asymptotic analysis at high wavenumber.

https://doi.org/10.1017/S0022112098008611 Published online by Cambridge University Press

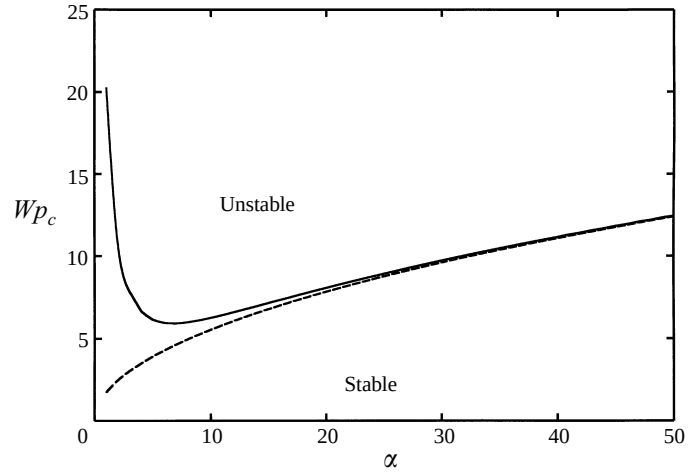


FIGURE 1. Neutral curve for axisymmetric CC flow. Solid curve: numerical result, $S = 0, N = 32$. Dashed curve: lower bound determined from asymptotic analysis at large α.

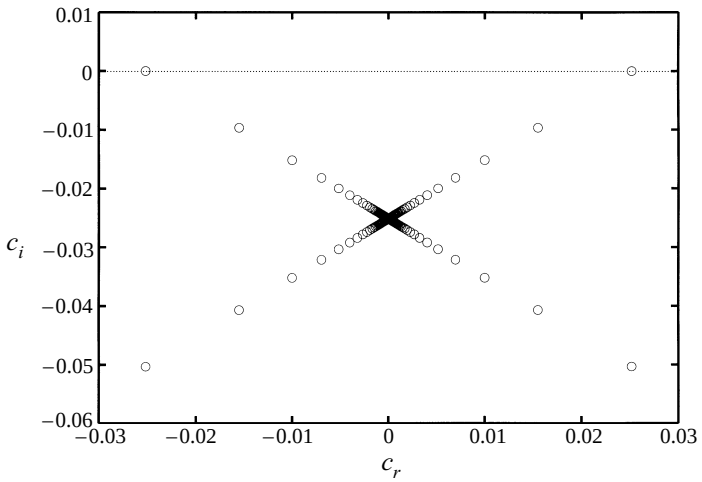


FIGURE 2. Spectrum of CC flow, $Wp = 5.93$, $\alpha = 6.7$, $\tilde{n} = 0$, $N = 64$.

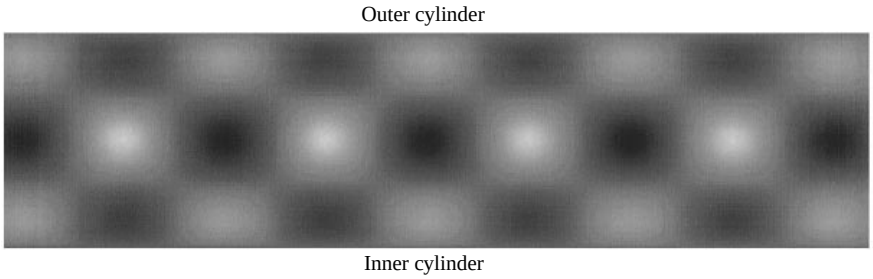


FIGURE 3. Snapshot of an azimuthal cross-section of the structure of $\tilde{\tau}_{\theta\theta}$, the $\theta\theta$-component of the destabilizing disturbance stress at $We_z = 0$, $Wp = 5.93$, $\alpha = 6.7$, $\tilde{n} = 0$, $N = 64$. The disturbance is an equal superposition of the eigenfunctions corresponding to the eigenvalues on the real axis on figure 2. Black indicates negative deviation from the steady-state value, white positive. Fluctuations travel radially, but not axially in this case.

https://doi.org/10.1017/S0022112098008611 Published online by Cambridge University Press

3.2. *Effect of axial shear flow*

3.2.1. *Scaling results for* $We_z \gg 1$

Axial flow introduces new stresses into the problem, which potentially change the dominant balances in the momentum equations. To begin the examination of the effect of axial flow, we consider the scaling behaviour when $We_z \gg 1$ in the CCAC case, where the base-state stresses are uniform across the gap. The primary question we address is: how large must Wp be for $\hat{\tau}_{\theta\theta}$ to enter into the leading-order radial momentum balance?

We first examine the case $We_z \gg 1, \alpha = O(1), \tilde{n} = 0$ and assume that Wp scales as We_z^m, where m is as yet unknown. The value of S has no effect on the scalings. Beginning with the rr-component of the linearized constitutive equation, and absorbing a factor of Wp into the velocities (including c), it is found that a balance between all terms in the equation is maintained if $c = O(1)$, $\hat{\tau}_{rr} = O(We_z)$ and if $1 - \rho = O(We_z^{-1})$. Evidently, there is a boundary layer of thickness We_z^{-1} near the outer cylinder. (Consideration of wave speeds of $O(We_z)$, reveals a boundary layer scale near the inner cylinder.) The scalings for the other stresses within this boundary layer can be obtained similarly: $\hat{\tau}_{r\theta} = O(We_z^{1+m}), \hat{\tau}_{rz} = O(We_z^2), \hat{\tau}_{\theta\theta} = O(We_z^{1+2m}), \hat{\tau}_{\theta z} = O(We_z^{2+m})$, $\hat{\tau}_{zz} = O(We_z^3)$. The existence of a boundary layer and the stress scalings are consistent with the analysis of Renardy (1997). All of the terms that couple base-state and disturbance quantities remain in the dominant balance for the constitutive equations. In the θ-vorticity equation, the dominant terms are $-\hat{\tau}_{rz}''$ and $i\alpha\tau_{zz}'$, which scale as We_z^4 in the boundary layer. For $\hat{\tau}_{\theta\theta}$, scaling as We_z^{1+2m}, to remain in the dominant balance, m must equal $3/2$. Thus, at fixed α, axisymmetric disturbances are not expected to be destabilizing until $Wp = O(We_z^{3/2})$. Axial flow provides very significant stabilization.

Similar analyses can be performed in a variety of relevant cases. For axisymmetric modes, three scaling regimes are found, depending on α:

$$\alpha We_z \gg 1: \qquad Wp = O(\alpha^{1/2} We_z^{3/2}), \tag{3.2}$$

$$We_z \gg 1, \alpha We_z = O(1): \qquad Wp = O(We_z), \tag{3.3}$$

$$We_z \gg 1, \alpha We_z \ll 1: \qquad Wp = O(\alpha^{-1}). \tag{3.4}$$

Boundary layers do not arise in the latter two cases. These results suggest that the minimum Wp for instability, $Wp_{c,min}$, and the wavelength $(2\pi/\alpha_{min})$, should increase linearly with We_z. The numerical results presented below are in good agreement with the scaling predictions, even for We_z as small as about unity. For non-axisymmetric perturbations ($\tilde{n} = O(1)$), with for example $\alpha = O(1)$, the dominant balance in the θ-vorticity equation is between $\hat{\tau}_{\theta z}'$ and $\hat{\tau}_{zz}'$, which are now $O(We_z^{2m+2})$, yielding $m = 2$. The three regimes present for axisymmetric modes are absent here; $m = 2$ is the weakest scaling found. Thus non-axisymmetric disturbances are even more strongly suppressed than axisymmetric ones, a result also confirmed by the numerical results. Furthermore, as $\tilde{n} \to \infty$, no power-law dependence of Wp on We_z can keep $\hat{\tau}_{\theta\theta}$ in the dominant balance, consistent with the result found above that when $n = O(\epsilon^{-1})$, We_θ must be $O(\epsilon^{-1})$ for instability. In summary, the scaling analysis predicts that for CCAC flow, $Wp_c = O(We_z)$, with axisymmetric modes being most dangerous. Since the actual azimuthal Weissenberg number We_θ is $O(\epsilon^{-1/2})$, these results suggest that an axial Weissenberg number much smaller than the azimuthal one can have a significant effect on the stability of the flow.

https://doi.org/10.1017/S0022112098008611 Published online by Cambridge University Press

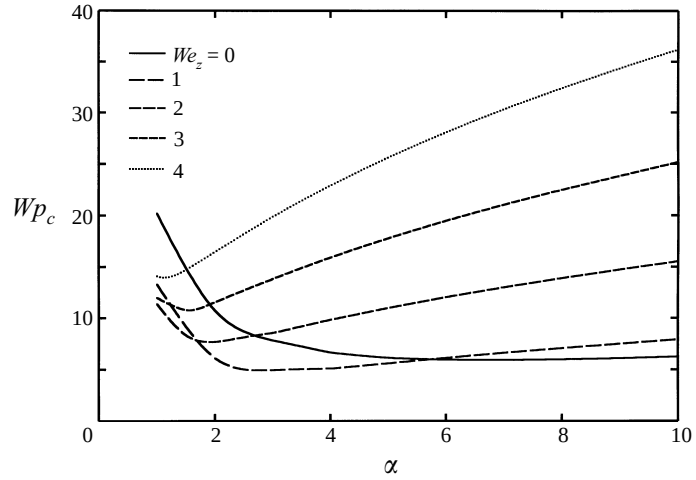


FIGURE 4. Neutral curve for CCAC flow, $S = 0$, $\tilde{n} = 0$, $N = 64$, at a number of values of We_z.

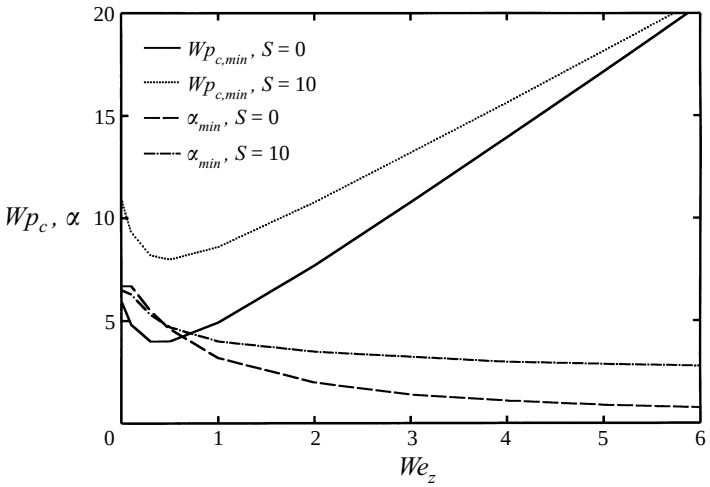


FIGURE 5. Dependence of $Wp_{c,min}$ and α_{min} on We_z in axisymmetric CCAC flow.

3.2.2. *Effect of axial Couette flow: linear analysis*

Figure 4 shows numerically determined axisymmetric neutral curves for the CCAC case with $S = 0$, at a number of values of We_z. Although Wp_c decreases for small We_z, once $We_z \gtrsim 1$, $Wp_{c,min}$ is greater than when $We_z = 0$. At constant α, the values for Wp_c closely follow the scaling prediction $Wp_c = O(We_z^{3/2})$. The dependence of $Wp_{c,min}$ on We_z is shown in figure 5; after an initial decrease, $Wp_{c,min}$ increases linearly with We_z, with a slope of about 3.2. Figure 5 also shows that α_{min} decreases monotonically with increasing We_z. In fact, when $We_z \gtrsim 1$, $\alpha We_z \approx 4.7$ at criticality, independently of We_z, in close agreement with the scalings described above for the regime $\alpha We_z = O(1)$. The corresponding curves for $S = 10$ are also shown on figure 5; the results are qualitatively identical. Since neither numerical results nor scaling analysis show any qualitative dependence on S, only results for $S = 0$ will be presented in the remainder of the paper.

https://doi.org/10.1017/S0022112098008611 Published online by Cambridge University Press

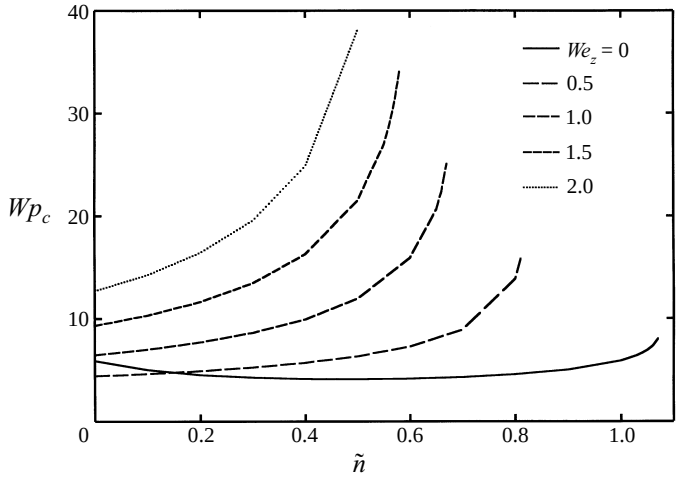


FIGURE 6. Dependence of Wp_c on azimuthal wavenumber $\tilde{n}$ in CCAC flow; $\alpha = 6.7$, $S = 0, N = 64$.

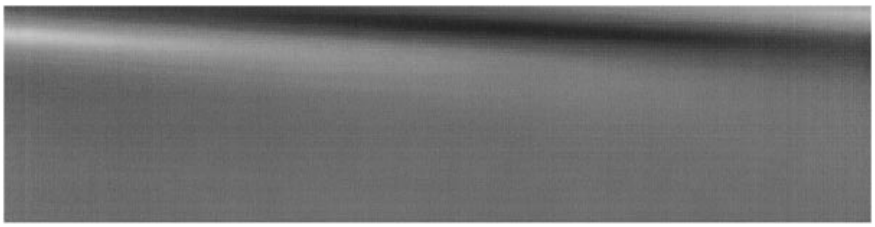


FIGURE 7. Snapshot of an azimuthal cross-section of $\tilde{\tau}_{\theta\theta}$ at $Wp = 13.95$, $\alpha = 1.1$, $\tilde{n} = 0$, $We_z = 4$, $N = 64$, CCAC flow. The disturbance travels without distortion to the right with speed $c = 3.37 \times 10^{-2}$.

The scaling results suggest that non-axisymmetric disturbances are strongly suppressed by axial flow. Figure 6 shows results of the numerical computation of Wp_c as a function of $\tilde{n}$ for $\alpha = 6.7, S = 0$. When $We_z = 0$, the minimum in this slice of the neutral surface appears near $\tilde{n} = 0.5$, showing that, in the narrow gap limit, CC flow is most unstable with respect to non-axisymmetric disturbances. This result is consistent with finite-gap calculations of Avgousti & Beris (1993*a*) and Joo & Shaqfeh (1994). As We_z increases, however, non-axisymmetric disturbances are strongly suppressed; at $We_z = 0.5$ axisymmetric disturbances are already the most dangerous. Results for Wp_c at fixed $\tilde{n}$ are in good agreement with the predicted We_z^2 dependence, and furthermore, as $\tilde{n}$ increases, the neutral curves turn sharply upward. Reliable computations at $N = 64$ were not possible above the endpoints of the curves shown, because Wp_c rapidly became so large that spurious instabilities occurred before real ones. These results are consistent with a scaling argument that shows that when $\tilde{n} \gg 1$, no power-law dependence of Wp on We_z can bring $\hat{\tau}_{\theta\theta}$ into the leading-order momentum balance.

Figure 7 shows $\tilde{\tau}_{\theta\theta}$ for a typical disturbance structure at instability. Parameter values are $We_z = 4, \alpha = 1.1, Wp = 13.95, S = 0, \tilde{n} = 0$; this is at the minimum of the axisymmetric neutral curve for $We_z = 4$. The disturbance is a travelling wave in the axial direction; stress fluctuations are localized near the outer cylinder, in contrast to the CC case, where they have uniform amplitude throughout the domain. This

https://doi.org/10.1017/S0022112098008611 Published online by Cambridge University Press

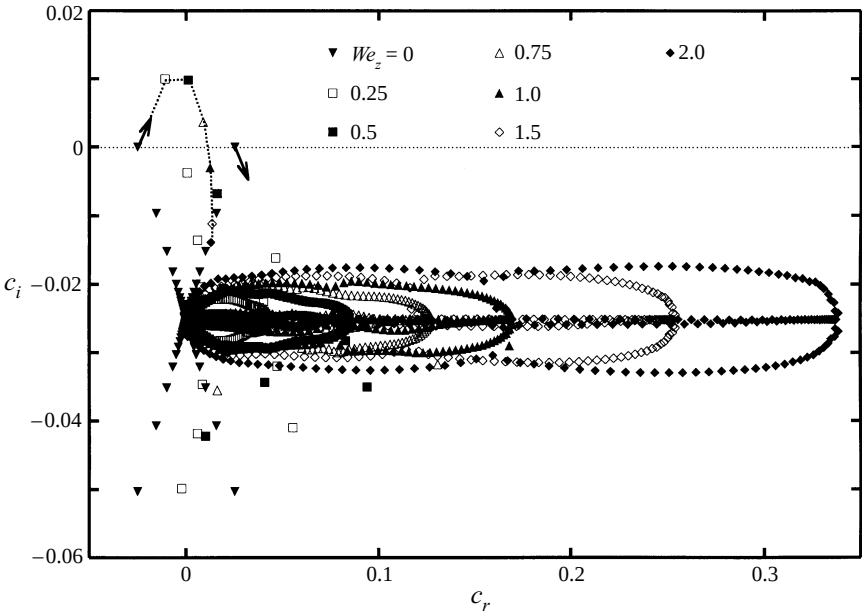


FIGURE 8. Evolution of the spectrum of CCAC flow as We_z increases, for $Wp = 93$, $\alpha = 6.7$, $\tilde{n} = 0$, $N = 64$.

localization is consistent with the scaling analysis, which predicts stress boundary layers when $\alpha = O(1)$. At these conditions the velocity field is not localized.

The CCAC flow is a hybrid between pure azimuthal shear flow and pure axial shear flow. Insight into the relationship between the stability problems in these limiting cases can be gained by looking at the spectra of CCAC flow as parameters change. Because of the scaling and numerical results, and the existence of a version of Squire's theorem for axial shear flow in the limit $\epsilon \to 0$ (Tlapa & Bernstein 1970), only axisymmetric disturbances need be considered. Figure 8 shows how the spectrum evolves when $Wp = 5.93, \alpha = 6.7, S = 0, \tilde{n} = 0$ as We_z increases from zero. The initial effect of axial Couette flow on the most unstable modes is to move the leftmost one upward and to the right, and the rightmost one downward and to the right, as shown by the arrows. Notice that at $We_z = 0.25$, for example, the leftmost eigenvalue is unstable, but has negative real part. Thus the destabilizing disturbance in this case travels upstream, in the direction opposite to the imposed axial flow. At higher We_z, the real part of the wave speed for this mode becomes positive (the disturbance travels downstream) and the imaginary part decreases below zero, resulting in stability. Its path is shown by the dotted curve. Numerically, the continuous spectrum is approximated by a ring of discrete eigenvalues (see the discussion in Appendix A); the figure shows the evolution of this as We_z increases. Now consider the evolution of the spectrum with $We_z = 2, \alpha = 6.7, S = 0, \tilde{n} = 0$, as Wp decreases, as shown in figure 9. In this case the spectra are scaled by Wp/We_z, so that the continuous spectrum has real parts spanning [0, 1]. As Wp decreases, the destabilizing eigenvalue moves downward, as again shown by the dotted curve, evolving into the leftmost Gorodtsov–Leonov eigenvalue of plane Couette flow as $Wp \to 0$ (see Figure 16). So although the Gorodtsov–Leonov eigenvalues do not lead to instability in plane shear flow, one of them is the source of instability in the hybrid CCAC flow and ultimately in pure CC flow.

https://doi.org/10.1017/S0022112098008611 Published online by Cambridge University Press

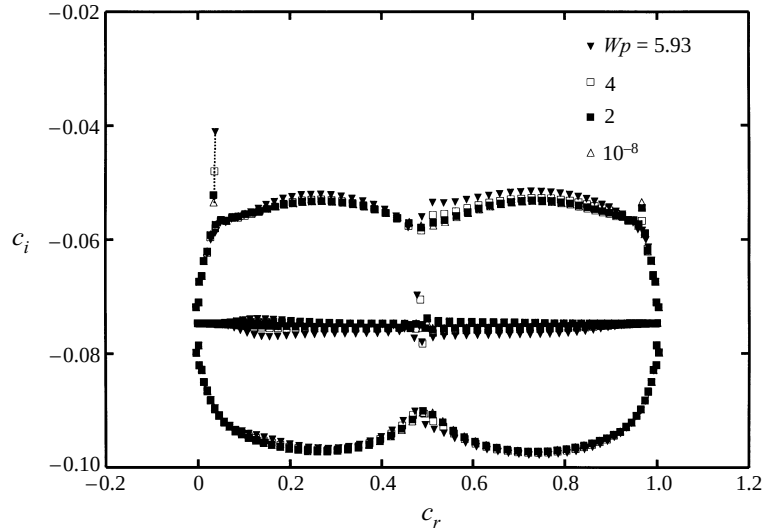


FIGURE 9. Evolution of the spectrum of CCAC flow as Wp decreases, for $We_z = 2$, $\alpha = 6.7$, $\tilde{n} = 0$, $N = 64$.

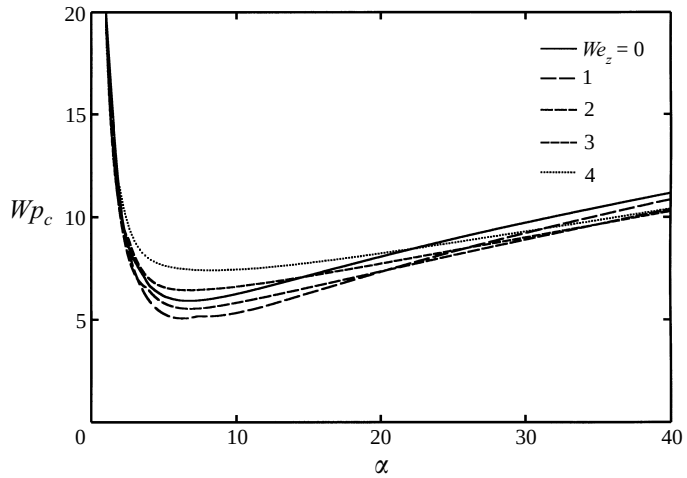


FIGURE 10. Neutral curve for CCAP flow, $S = 0$, $\tilde{n} = 0$, $N = 64$, at a number of values of We_z.

3.2.3. *Effect of axial Poiseuille flow: linear analysis*

Figure 10 shows neutral curves for the CCAP case with $S = 0, \tilde{n} = 0$ at various We_z. Figure 11 shows the dependence of $Wp_{c,min}$ on We_z. Results for $S \neq 0$ are qualitatively identical. In some of the neutral curves, there are noticeable kinks (and a corresponding jump in α_{min}); in contrast to the CCAC case, the identity of the most unstable eigenvalue changes with α and We_z (see below). As in the CCAC case, the flow is stabilized once We_z is sufficiently large, but the effect is not nearly as dramatic as it is in the CCAC case.

The behaviour of non-axisymmetric disturbances to CCAP flow is similar to that in the CCAC case. Figure 12 shows the dependence of Wp_c on $\tilde{n}$ when $S = 0, \alpha = 6.7$. Above $We_z = 1$, axisymmetric modes are the most unstable, although here the neutral

https://doi.org/10.1017/S0022112098008611 Published online by Cambridge University Press

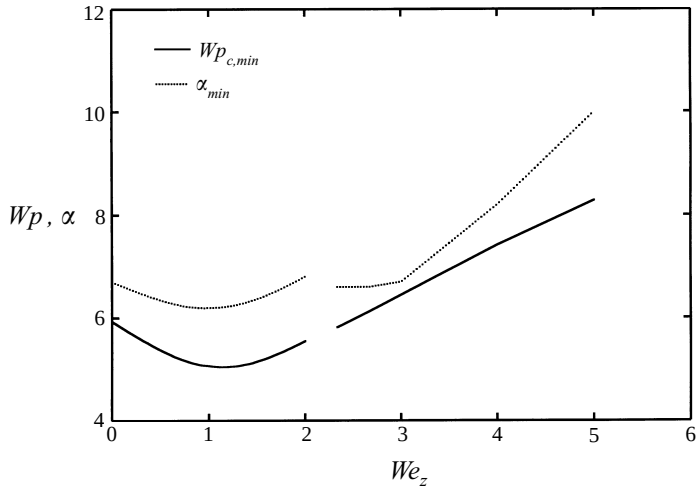


FIGURE 11. Dependence of $Wp_{c,min}$ and α_{min} on We_z in CCAP flow, $S = 0$, $\tilde{n} = 0$, $N = 64$. The identity of the most unstable eigenvalue changes between $We_z = 2$ and $We_z = 2.3$.

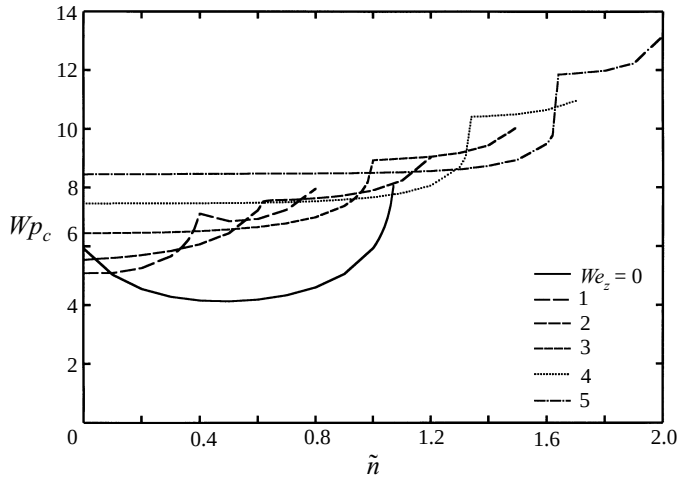


FIGURE 12. Dependence of Wp_c on azimuthal wavenumber $\tilde{n}$ in CCAP flow; $\alpha = 6.7$, $S = 0, N = 64$.

surface initially appears flat on the scale chosen for the figure. The kinks in the curve show where the most dangerous mode changes identity, and as in the CCAC case, the curves turn up sharply, becoming difficult to compute, as $\tilde{n}$ increases.

As in the CCAC case, the destabilizing disturbances in CCAP flow are travelling waves. However, their radial structure differs significantly. Figure 13 shows $\tilde{\tau}_{\theta\theta}$ at $We_z = 4, \alpha = 8.2, \tilde{n} = 0, Wp = 7.419$; this is at the minimum of the axisymmetric neutral curve for $We_z = 4$. The fluctuations are again localized, but now in the centre of the annular domain, and they travel with a speed very near the fluid axial velocity at the centreline. Near the centreline the axial shear rate and corresponding stresses are virtually zero, so the dominant balance here remains that of the pure CC problem, while closer to the walls the axial stresses overwhelm the effect of $\hat{\tau}_{\theta\theta}$. An asymptotic analysis for high α, assuming the existence of an internal layer of thickness $1/\alpha$ centred at $\rho = 1/2$, yields a leading-order inner problem that is independent of We_z.

https://doi.org/10.1017/S0022112098008611 Published online by Cambridge University Press

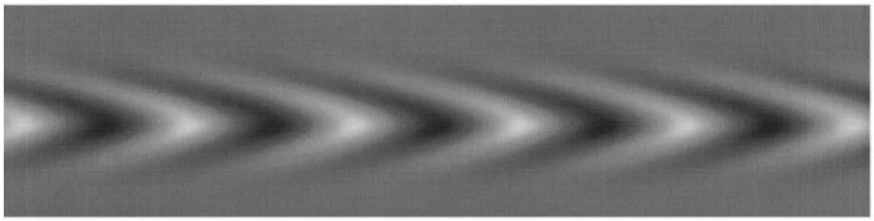


FIGURE 13. Azimuthal cross-section of the structure of $\tilde{\tau}_{\theta\theta}$ at $Wp = 7.419$, $\alpha = 8.2$, $\tilde{n} = 0$, $We_z = 4$, $N = 64$, CCAP flow. The disturbance travels without distortion to the right with speed $c = 0.144$, slightly faster than the steady-state centreline axial velocity of $1/Wp = 0.135$.

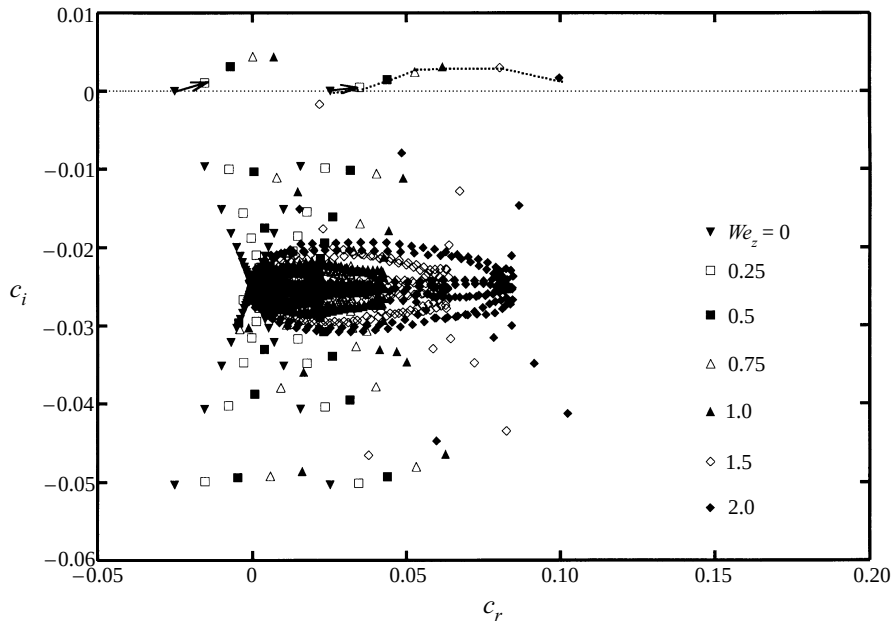


FIGURE 14. Evolution of the spectrum of CCAP flow as We_z increases, for $Wp = 5.93$, $\alpha = 6.7$, $\tilde{n} = 0$, $N = 64$.

This result is consistent with the numerical neutral curves, which nearly collapse to a single curve at high α and $O(1)$ We_z.

The internal layer structure of the most unstable disturbance at $O(1)$ We_z rules out identification of this mode with one of the Gorodtsov–Leonov modes, which are boundary layer modes. However, in plane Poiseuille (PP) flow another pair of discrete modes exists, which are shown in Appendix A to have an internal layer structure. We now examine the spectra as parameters change, to better understand the relationship between CCAP flow and pure PP flow. Figure 14 shows the evolution of the spectrum for $Wp = 5.93, \alpha = 6.7, \tilde{n} = 0$ as We_z varies. Both dominant eigenvalues of the pure CC flow are initially destabilized; initially the leftmost is most unstable, but the rightmost one becomes the most unstable once $We_z \gtrsim 1$. Its evolution is tracked by the dotted curve. This change also explains the kink in the neutral curves at fixed We_z as α increases. Figure 15 shows how the spectrum changes as Wp is decreased with $We_z = 2, \alpha = 6.7$; the destabilizing eigenvalue (dotted curve) relaxes to an internal layer mode of PP flow, mode (c) of figure 18, as $Wp \to 0$. So, as in the CCAC case,

https://doi.org/10.1017/S0022112098008611 Published online by Cambridge University Press

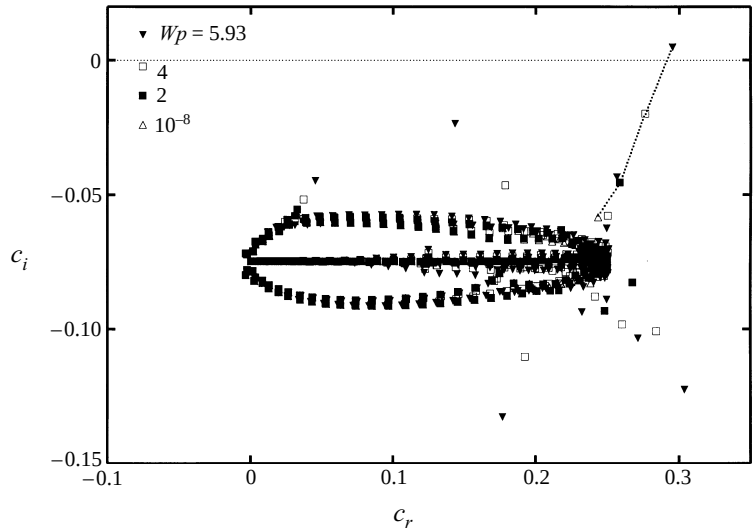


FIGURE 15. Evolution of the spectrum of CCAP flow as Wp decreases, for $We_z = 2$, $\alpha = 6.7$, $\tilde{n} = 0$, $N = 64$.

the destabilizing mode is related to a mode of a pure plane shear flow, but in this case an internal layer mode of PP flow rather than a Gorodtsov–Leonov mode.

3.3. *Nonlinear analysis*

In addition to the effect of axial flow on the position of bifurcation points, it is of interest to determine its effect on their criticality. In particular, if the goal of applying a secondary flow is to suppress instability, it is desirable to not only move the bifurcation point upward, but also to make it supercritical. Otherwise, instability to finite-amplitude disturbances can occur below the bifurcation point, leading to flows that are far from the desired state. With the approach described above, we have determined the criticality of bifurcations of both CCAC and CCAP flow at $Wp_{c,min}$ and α_{min} when $S = 0, \tilde{n} = 0$. The results are shown in table 1.

At $We_z = 0$, $\mu_2 < 0$, so from (2.8), the bifurcation to travelling waves is predicted to be subcritical: no stable non-trivial solution exists near the bifurcation point (Golubitsky *et al.* 1985; Sureshkumar *et al.* 1994). Simulations for finite gaps predict supercritical bifurcation (Northey *et al.* 1992; Avgousti *et al.* 1993; Avgousti & Beris 1993*b*). However, results from Sureshkumar *et al.* (1994) show that as the gap becomes smaller, bifurcations of non-axisymmetric states switch from supercritical to subcritical. Given the fact that axisymmetric and non-axisymmetric modes with $n = O(1)$ must behave identically as $\epsilon \to 0$ and that non-axisymmetric modes become subcritical as ϵ decreases, our prediction of subcriticality does not appear to be in conflict with existing results.

When $We_z \neq 0$, the CCAC and CCAP results differ qualitatively. For CCAC flow, $\mu_2 < 0$ for all of the values of We_z studied. In contrast, in CCAP flow, μ_2 changes from negative to positive as We_z increases; the discontinuity in μ_2 between $We_z = 2$ and $We_z = 3$ reflects the change in identity of the most dangerous mode as We_z increases. Axial Poiseuille flow both increases Wp_c and changes the bifurcation from subcritical to supercritical.

https://doi.org/10.1017/S0022112098008611 Published online by Cambridge University Press

	We_z	$Wp_{c,min}$	α_{min}	μ_2	ω_2
(*a*)	0	5.93	6.7	−0.306	1.56×10^{-3}
	1	4.94	3.2	−0.246	-6.90×10^{-3}
	2	7.70	2.0	−0.152	-3.31×10^{-3}
	3	10.79	1.4	-9.99×10^{-2}	-1.35×10^{-3}
	4	13.95	1.1	-6.60×10^{-2}	-6.02×10^{-4}
	5	17.18	0.9	-4.85×10^{-2}	-3.18×10^{-4}
	10	33.63	0.47	-1.91×10^{-2}	-4.54×10^{-5}
	We_z	$Wp_{c,min}$	α_{min}	μ_2	ω_2
(*b*)	0	5.93	6.7	−0.306	1.56×10^{-3}
	1	5.07	6.2	-1.52×10^{-2}	-5.83×10^{-3}
	2	5.55	6.8	0.210	6.60×10^{-3}
	3	6.45	6.6	0.122	4.72×10^{-3}
	4	7.42	8.2	0.138	1.22×10^{-2}

TABLE 1. Results of linear and weakly nonlinear analysis for (*a*) CCAC and (*b*) CCAP flows, $S = 0, \tilde{n} = 0, N = 64$.

3.4. *Mechanisms of stabilization and destabilization*

For axisymmetric disturbances to pure CC flow, the basic instability mechanism was elucidated by LSM and further illustrated using energy arguments by Joo & Shaqfeh (1992). In this case, a velocity perturbation that leads to local radial extension induces a perturbation radial normal stress $\tilde{\tau}_{rr}$. The rotation and deformation due to the steady-state azimuthal shear flow then act on the local radial stress to induce an azimuthal stress $\tilde{\tau}_{\theta\theta}$. This local increase in hoop stress leads to an unstable balance of forces in the radial momentum equation, as azimuthally stretched material presses inward. This unstable balance leads to further velocity perturbations and the propagation of the instability.

In both the CCAC and CCAP cases, axisymmetric flow is initially destabilized, then stabilized as We_z increases. We discuss here the mechanisms underlying these effects, considering axisymmetric perturbations of the CCAC flow of the upper-convected Maxwell fluid. Non-axisymmetric modes are not discussed, since only for small We_z are they most dangerous.

The stabilization mechanism when $We_z \gg 1$ is manifest in the change in dominant balance outlined in the scaling analysis above. For axisymmetric disturbances, the dominant stresses, with which $\tilde{\tau}_{\theta\theta}$ must compete, are $\tilde{\tau}_{rz}$ and $\tilde{\tau}_{zz}$. The scalings for these stresses arise from coupling of the base-state and disturbance quantities; all the coupling terms remain in the leading-order constitutive equations, showing that there is no single coupling that individually determines the sizes of these stresses. Nevertheless, to provide a heuristic view of the stabilization mechanism, we single out one of these terms, the contribution $2\bar{\tau}_{zz}\partial\tilde{v}_z/\partial z$ to $\tilde{\tau}_{zz}$. This term scales as We_z^2 (in the absence of a boundary layer) and reflects the fact that an elastic material under tension (e.g. a membrane, or in the present case an annular fluid element) resists deformation. The flow resists the radial deformation and corresponding axial gradients required for the elastic instability to grow. This explanation also describes why a negative second normal stress coefficient is stabilizing in the absence of axial flow: as long as $\bar{\tau}_{zz} > \bar{\tau}_{rr}$, radial deformation of fluid elements will be resisted. Finally, we can also qualitatively explain the change in wavenumber at instability

https://doi.org/10.1017/S0022112098008611 Published online by Cambridge University Press

as We_z increases. The instability moves to longer wavelengths because for a given amplitude of deformation, the force required to impose that deformation is smaller the longer the wavelength. A similar stabilization mechanism for high-Reynolds-number, high-Weissenberg-number free shear flows is discussed in Azaiez & Homsy (1994) (particularly the appendix by Hinch) and Rallison & Hinch (1995). In these works, the source of instability is completely different from that considered here, but the mechanism of stabilization is similar.

For the high-We_z behaviour, the scaling analysis provides *a priori* results, showing the change in the dominant balance that leads to stabilization. No change in dominant balance occurs when $We_z \ll 1$; effects here are more subtle, and to study the contributions of various terms, a scaling analysis is not useful. We will use an *a posteriori* analysis similar in spirit, but not detail, to an energy analysis (Serrin 1959; Feinberg & Schowalter 1969*a*, *b*; Joo & Shaqfeh 1992), to perform a term-by-term comparison of the contributions to the linear stability equations (cf. Steen & Aidun 1988; Graham & Steen 1991).

Consider the rr-component of the linearized constitutive equation:

$$\frac{\partial \tilde{\tau}_{rr}}{\partial t} = -\bar{v}_z \tilde{\tau}_{rr} + 2\bar{\tau}_{rz}\frac{\partial \tilde{v}_r}{\partial z} + 2\frac{\partial \tilde{v}_r}{\partial r} - \frac{1}{Wp}\tilde{\tau}_{rr}.$$

We define an inner product

$$(a,b) = \frac{\alpha}{2\pi}\int_0^1 \int_0^{2\pi/\alpha} a(\rho,z)\bar{b}(\rho,z)\sum_{k=0}^{N}\delta(\rho_k)\,\mathrm{d}\rho\,\mathrm{d}z,$$

and a norm $||u|| = (u,u)^{1/2}$, where $\rho_k = (1+\cos k\pi/N)/2$ is the position of the kth Chebyshev–Gauss–Lobatto collocation point. With this inner product, the integral over ρ becomes the sum over the collocation points. Taking the inner product of the rr-constitutive equation with $\tilde{\tau}_{rr}$ gives

$$\frac{1}{2}\frac{\mathrm{d}}{\mathrm{d}t}||\tilde{\tau}_{rr}||^2 = \left(\tilde{\tau}_{rr}, 2\bar{\tau}_{rz}\frac{\partial \tilde{v}_r}{\partial z}\right) + \left(\tilde{\tau}_{rr}, 2\frac{\partial \tilde{v}_r}{\partial r}\right) - \left(\tilde{\tau}_{rr}, \frac{1}{Wp}\tilde{\tau}_{rr}\right).$$

This is an evolution equation for the positive definite quantity $||\tilde{\tau}_{rr}||^2$; given the numerical solution, all the terms in the equation can be evaluated. In particular, the signs of the various contributions to the right-hand side of the equation determine whether they are destabilizing (> 0) or stabilizing (< 0). The convective term ($\tilde{\tau}_{rr}\bar{v}_z\partial\tau_{rr}/\partial z$) vanishes identically because $\tilde{\tau}_{rr}$ and its z-derivative are out of phase in z by $\pi/2$. Analogous equations can be constructed for the other stresses. Since the Reynolds number is zero, the vorticity equation is not an evolution equation. Nevertheless, performing the same operation will give information about which terms balance. For example, in the θ-vorticity equation, with $\tilde{\omega}_\theta$ being the θ-component of the disturbance vorticity, we have

$$0 = \left(\tilde{\omega}_\theta, \frac{\partial^2 \tilde{\tau}_{rr}}{\partial r \partial z}\right) + \left(\tilde{\omega}_\theta, \frac{\partial^2 \tilde{\tau}_{rz}}{\partial z^2}\right) - \left(\tilde{\omega}_\theta, \frac{\partial^2 \tilde{\tau}_{rz}}{\partial r^2}\right) - \left(\tilde{\omega}_\theta, \frac{\partial \tilde{\tau}_{\theta\theta}}{\partial z}\right) - \left(\tilde{\omega}_\theta, \frac{\partial^2 \tilde{\tau}_{zz}}{\partial r \partial z}\right).$$

The fourth term is the hoop stress contribution to the radial momentum balance.

Table 2 shows the terms on the right-hand sides of the equations at $We_z = 0$ and $We_z = 0.01$, when $\alpha = 6.7, Wp = 5.93$, evaluated at $t = 0$. Evaluation of the terms at a different time does not change their relative magnitudes. For the $We_z = 0$ case, the terms in each equation sum to zero, because the flow is marginally stable, while at $We_z = 0.01$, the sums of terms in the constitutive equations are positive,

https://doi.org/10.1017/S0022112098008611 Published online by Cambridge University Press

since the flow is unstable. Consider first the $We_z = 0$ column. We see that $\tilde{\tau}_{\theta\theta}$ makes the largest individual contribution to the θ-vorticity equation. In agreement with the arguments of LSM, the driving force for the production of hoop stresses can be seen from the table to be the interaction of base-state velocity gradients with disturbance stresses: the term $(\tilde{\tau}_{\theta\theta}, 2\partial\bar{v}_\theta/\partial r\tilde{\tau}_{r\theta})$ in the $\theta\theta$-equation. The main source of the shear stress perturbation is the couping of $\partial\bar{v}_\theta/\partial r$ with $\tilde{\tau}_{rr}$, where $\tilde{\tau}_{rr}$ arises from extensional velocity perturbations. The initial destabilizing effect of axial flow can be seen from column 2 of table 2. The hoop stress still dominates the θ-vorticity equation. In each component of the constitutive equation, the terms due to the coupling of the base-state axial stresses $\bar{\tau}_{rz}, \bar{\tau}_{\theta z}, \bar{\tau}_{zz}$ with velocity perturbations have a net destabilizing effect. Paradoxically, these same terms contribute to the stress scalings that lead to stabilization at high We_z. The resolution to the paradox lies in the change in dominant balance in the momentum equation. As noted, very little changes here between $We_z = 0$ and $We_z = 0.01$. However, at $We_z = 2$, and all other parameters unchanged, the same calculation, for the least slowly decaying mode, shows that the contribution of $\tilde{\tau}_{\theta\theta}$ is already negligible, an order of magnitude smaller than the dominant terms. Thus, this *a posteriori* analysis corroborates the scaling arguments once We_z is sufficiently large.

4. Conclusions

Scaling arguments and computations with the upper-convected Maxwell and Oldroyd-B constitutive equations in the narrow gap limit predict that superimposed axial Couette or Poiseuille flow can have a significant effect on the stability and bifurcation behaviour of viscoelastic circular Couette flow. For superimposed Couette flow, scaling arguments predict that the critical azimuthal Weissenberg number should increase as We_z^1 for axisymmetric modes, and We_z^2 for non-axisymmetric ones. The stabilizing effect is associated with the axial stresses induced by the secondary flows, which control the dominant balances in the momentum equation at large We_z. Numerical results show that although axisymmetric modes are destabilized at small We_z, through a coupling between velocity perturbations and base-state stresses, these scalings hold when We_z is sufficiently large, and axisymmetric disturbances are thus the most dangerous. Similar observations hold for superimposed Poiseuille flow, although the degree of stabilization is smaller because the axial stresses are not uniformly large. Weakly nonlinear analysis shows that the axisymmetric instability is subcritical in the narrow gap limit when $We_z = 0$, but that axial Poiseuille flow can make the bifurcation supercritical. When We_z is sufficiently large, the stress fluctuations are localized, and can be thought of in terms of a boundary layer instability in the Couette flow case, and an internal layer instability in the Poiseuille case.

From the mathematical point of view, the present results illustrate the unity of the stability problems for a number of flows. The most unstable eigenvalue of the axisymmetric problem when axial Couette flow is superimposed on circular Couette flow reduces to one of the Gorodtsov–Leonov eigenvalues (corresponding to a boundary-localized fluctuation) in the plane Couette limit. If axial Poiseuille flow is superimposed, the most unstable eigenvalue reduces to an internally localized mode in the discrete spectrum of plane Poiseuille flow.

An important practical implication of this work is that it points to a strategy for improving the stability of viscoelastic flows, by imposing a relatively small secondary flow in either an open loop or closed loop manner. In coating operations, for example,

https://doi.org/10.1017/S0022112098008611 Published online by Cambridge University Press

Term	$We_z = 0$	$We_z = 0.01$
$\left(\tilde{\tau}_{rr}, 2\bar{\tau}_{rz}\dfrac{\partial\tilde{v}_r}{\partial z}\right)$	0	3.14×10^{-4}
$\left(\tilde{\tau}_{rr}, 2\dfrac{\partial\tilde{v}_r}{\partial r}\right)$	3.28×10^{-2}	3.55×10^{-2}
$\left(\tilde{\tau}_{rr}, -Wp^{-1}\tilde{\tau}_{rr}\right)$	-3.28×10^{-2}	-3.51×10^{-2}
$\left(\tilde{\tau}_{r\theta}, \dfrac{\partial\bar{v}_\theta}{\partial r}\tilde{\tau}_{rr}\right)$	0.866	0.930
$\left(\tilde{\tau}_{r\theta}, \bar{\tau}_{\theta z}\dfrac{\partial\tilde{v}_r}{\partial z}\right)$	0	5.61×10^{-3}
$\left(\tilde{\tau}_{r\theta}, \bar{\tau}_{rz}\dfrac{\partial\tilde{v}_\theta}{\partial z}\right)$	0	-4.11×10^{-3}
$\left(\tilde{\tau}_{r\theta}, \dfrac{\partial\tilde{v}_\theta}{\partial r}\right)$	−0.433	−0.461
$\left(\tilde{\tau}_{r\theta}, \bar{\tau}_{r\theta}\dfrac{\partial\tilde{v}_r}{\partial r}\right)$	0.289	0.321
$\left(\tilde{\tau}_{r\theta}, -Wp^{-1}\tilde{\tau}_{r\theta}\right)$	−0.722	−0.774
$\left(\tilde{\tau}_{rz}, \dfrac{\partial\bar{v}_z}{\partial r}\tilde{\tau}_{rr}\right)$	0	-2.32×10^{-5}
$\left(\tilde{\tau}_{rz}, \bar{\tau}_{zz}\dfrac{\partial\tilde{v}_r}{\partial z}\right)$	0	1.11×10^{-6}
$\left(\tilde{\tau}_{rz}, \dfrac{\partial\tilde{v}_r}{\partial z}\right)$	4.51×10^{-3}	5.56×10^{-3}
$\left(\tilde{\tau}_{rz}, \dfrac{\partial\tilde{v}_z}{\partial r}\right)$	1.55×10^{-2}	1.70×10^{-2}
$\left(\tilde{\tau}_{rz}, -Wp^{-1}\tilde{\tau}_{rz}\right)$	-2.00×10^{-2}	-2.20×10^{-2}
$\left(\tilde{\tau}_{\theta\theta}, 2\dfrac{\partial\bar{v}_\theta}{\partial r}\tilde{\tau}_{r\theta}\right)$	10.2	10.8
$\left(\tilde{\tau}_{\theta\theta}, 2\bar{\tau}_{\theta z}\dfrac{\partial\tilde{v}_\theta}{\partial z}\right)$	0	2.09×10^{-3}
$\left(\tilde{\tau}_{\theta\theta}, 2\bar{\tau}_{r\theta}\dfrac{\partial\tilde{v}_\theta}{\partial r}\right)$	4.74×10^{-5}	−0.360
$\left(\tilde{\tau}_{\theta\theta}, -Wp^{-1}\tilde{\tau}_{\theta\theta}\right)$	−10.2	−10.3

Term	$We_z = 0$	$We_z = 0.01$
$\left(\tilde{\tau}_{\theta z}, \dfrac{\partial\bar{v}_z}{\partial r}\tilde{\tau}_{r\theta}\right)$	0	-7.92×10^{-3}
$\left(\tilde{\tau}_{\theta z}, \dfrac{\partial\bar{v}_\theta}{\partial r}\tilde{\tau}_{rz}\right)$	0.816	0.873
$\left(\tilde{\tau}_{\theta z}, \bar{\tau}_{zz}\dfrac{\partial\tilde{v}_\theta}{\partial z}\right)$	0	7.91×10^{-5}
$\left(\tilde{\tau}_{\theta z}, \dfrac{\partial\tilde{v}_\theta}{\partial z}\right)$	0.375	0.396
$\left(\tilde{\tau}_{\theta z}, \bar{\tau}_{rz}\dfrac{\partial\tilde{v}_\theta}{\partial r}\right)$	0	4.73×10^{-3}
$\left(\tilde{\tau}_{\theta z}, \bar{\tau}_{\theta z}\dfrac{\partial\tilde{v}_z}{\partial z}\right)$	0	6.53×10^{-3}
$\left(\tilde{\tau}_{\theta z}, \bar{\tau}_{r\theta}\dfrac{\partial\tilde{v}_z}{\partial r}\right)$	0.794	0.889
$\left(\tilde{\tau}_{\theta z}, -Wp^{-1}\tilde{\tau}_{\theta z}\right)$	−1.99	−2.11
$\left(\tilde{\tau}_{zz}, 2\dfrac{\partial\bar{v}_z}{\partial r}\tilde{\tau}_{rz}\right)$	0	5.97×10^{-5}
$\left(\tilde{\tau}_{zz}, 2\dfrac{\partial\tilde{v}_z}{\partial z}\right)$	3.28×10^{-2}	3.57×10^{-2}
$\left(\tilde{\tau}_{zz}, 2\bar{\tau}_{zz}\dfrac{\partial\tilde{v}_z}{\partial z}\right)$	0	7.13×10^{-6}
$\left(\tilde{\tau}_{zz}, \bar{\tau}_{rz}\dfrac{\partial\tilde{v}_z}{\partial r}\right)$	0	3.76×10^{-4}
$\left(\tilde{\tau}_{zz}, -Wp^{-1}\tilde{\tau}_{zz}\right)$	-3.28×10^{-2}	-3.53×10^{-2}
$\left(\tilde{\omega}_r, \dfrac{\partial^2\tilde{\tau}_{r\theta}}{\partial r\partial z}\right)$	−16.8	−17.8
$\left(\tilde{\omega}_r, \dfrac{\partial^2\tilde{\tau}_{\theta z}}{\partial z^2}\right)$	16.8	17.8
$\left(\tilde{\omega}_\theta, \dfrac{\partial^2\tilde{\tau}_{rr}}{\partial r\partial z}\right)$	−2.36	−2.56
$\left(\tilde{\omega}_\theta, \dfrac{\partial^2\tilde{\tau}_{rz}}{\partial z^2}\right)$	0.337	0.336
$\left(\tilde{\omega}_\theta, -\dfrac{\partial^2\tilde{\tau}_{rz}}{\partial r^2}\right)$	0.650	0.825
$\left(\tilde{\omega}_\theta, -\dfrac{\partial\tilde{\tau}_{\theta\theta}}{\partial z}\right)$	3.74	3.97
$\left(\tilde{\omega}_\theta, -\dfrac{\partial^2\tilde{\tau}_{zz}}{\partial r\partial z}\right)$	−2.36	−2.58

TABLE 2. Contributions of individual terms to the evolution of the most dangerous disturbance, $S = 0, \tilde{n} = 0, \alpha = 6.7, Wp = 5.93$, at $We_z = 0$ and $We_z = 0.01$. The horizontal lines separate the terms in different equations.

https://doi.org/10.1017/S0022112098008611 Published online by Cambridge University Press

motion of a boundary or an imposed pressure gradient in the transverse direction may lead to significant stability improvements.

This work was supported through a Shell Faculty Fellowship, an NSF CAREER award, CTS-9502677 and an ACS/PRF starter grant, 28997-G9. The author gratefully acknowledges helpful discussions with M. Renardy, who clarified the structure of solutions at a singular point, and with A. N. Beris.

Appendix A. The structure of the spectrum of viscoelastic plane shear flow

This Appendix briefly reviews previous work and presents some original results regarding the properties of the exact and (Chebyshev) discretized spectra of the linear stability problems for inertialess plane Couette and Poiseuille flows of an upper-convected Maxwell fluid. The appropriately non-dimensionalized governing equations for these cases can be obtained from the equations of Appendix B by rescaling all velocities (including the wave speed c) by We_z/Wp and letting $Wp \to 0$. Only axisymmetric (two-dimensional) perturbations need be considered in this limit, as a version of Squire's theorem guarantees that these are the most dangerous disturbances (Tlapa & Bernstein 1970).

Gorodtsov & Leonov (1967) analytically determined the spectrum for plane Couette (PC) flow of the UCM fluid, reducing the problem to a fourth-order ODE for the stream function (which is proportional to $\hat{v}_r$). For the case where the inner cylinder (corresponding to the lower wall in the usual plane flow geometry) is moving, this equation is

$$\left[Q(\rho,c)^2\mathrm{D}^2 - \alpha^2 Q(\rho,c)^2 + 2 + 2Q(\rho,c)\mathrm{D}\right]\left[\mathrm{D}^2 - 2\mathrm{i}\alpha We_z\mathrm{D} - \alpha^2(1+2We_z^2)\right]\hat{v}_r = 0, \tag{A 1}$$

where $\mathrm{D} = \mathrm{d}/\mathrm{d}\rho$ and $Q(\rho,c) = -c + (1-\rho) - \mathrm{i}/(\alpha We_z)$. The spectrum consists of two discrete eigenvalues, the so-called Gorodtsov–Leonov eigenvalues, and a continuous spectrum, which lies in the negative (stable) half-plane and corresponds to the values of c where $Q = 0$: i.e. the strip $\{c = (1-\rho_0) - \mathrm{i}/(\alpha We_z)\ \forall \rho_0 \in [0,1]\}$. At these values of c, the equation exhibits a regular singular point at the position $\rho = \rho_0$. The eigenfunctions corresponding to these values of c will be constructed below. Figure 16 shows an example of the numerically determined spectrum, computed with the method used in the main text (with and without boundary regularization). There is a clear difference in the resolution of the discrete and continuous components of the spectrum. The discrete eigenvalues are approximated to very high accuracy, while the continuous spectrum is not approximated nearly as well.

The origin of the poor numerical approximation of the continuous spectrum lies in the structure of the exact eigenfunctions. Gorodtsov & Leonov explicitly constructed only the eigenfunctions corresponding to the discrete eigenvalues. These eigenvectors are C^∞ and are thus easily computed with a Chebyshev spectral discretization. For values of c in the continuous spectrum, the solution behaviour at the singular point is the key to understanding the numerical results. From above, $c = 1 - \rho_0 - \mathrm{i}/(\alpha We_z)$. Let $\varrho = \rho - \rho_0$, so $Q = -\varrho$. Now (A 1) becomes

$$\left[\varrho^2\mathrm{D}^2 - \alpha^2\varrho^2 + 2 - 2\varrho\mathrm{D}\right]\left[\mathrm{D}^2 - 2\mathrm{i}\alpha We_z\mathrm{D} - \alpha^2(1+2We_z^2)\right]\hat{v}_r = 0. \tag{A 2}$$

We now take $\hat{v}_r$ to be a function of ϱ. The stresses can be written in terms of $\hat{v}_r(\varrho)$:

https://doi.org/10.1017/S0022112098008611 Published online by Cambridge University Press

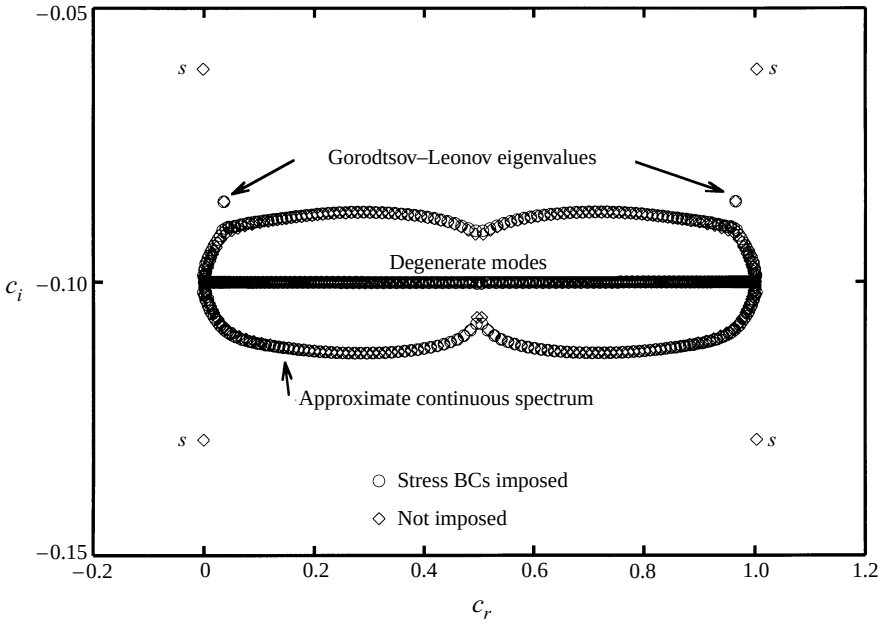


FIGURE 16. Numerical spectrum of plane Couette flow, $We_z = 1$, $\alpha = 10$, $N = 128$, with and without boundary regularization. The spurious eigenvalues obtained when boundary regularization is not used are marked *s*. This spectrum was obtained with the code used in the main text, with Wp set to 1×10^{-8} and the spectrum rescaled by We_z/Wp. The approximate continuous spectrum is the ring of eigenvalues indicated. The eigenvalues lying exactly on $c_i = -0.10$ are degenerate, arising from the fact that $\hat{\tau}_{r\theta}, \hat{\tau}_{\theta\theta}$ and $\hat{\tau}_{\theta z}$ remain in the formulation, but are identically zero in the PC and PP limits.

to leading order near $\varrho = 0$,

$$\hat{\tau}_{rr}(\varrho) \sim \frac{2}{\alpha}\frac{\alpha We_z \hat{v}_r(0) + \mathrm{i}\hat{v}_r'(0)}{\varrho}, \tag{A 3a}$$

$$\hat{\tau}_{rz}(\varrho) \sim \frac{2}{\alpha^2}\frac{-\mathrm{i}\alpha We_z \hat{v}_r(0) + \hat{v}_r'(0)}{\varrho^2}, \tag{A 3b}$$

$$\hat{\tau}_{zz}(\varrho) \sim \frac{2}{\alpha^3}\frac{-2\alpha We_z \hat{v}_r(0) - 2\mathrm{i}\hat{v}_r'(0)}{\varrho^3}. \tag{A 3c}$$

Clearly, unless $\hat{v}_r(0)$ and $\hat{v}_r'(0)$ vanish, the stresses will be very singular.

Previous approximate analyses of this problem have been performed by Keiller (1992) and Sureshkumar & Beris (1995*b*), but neither of these elucidated the exact local structure of the solution. Keiller performed a partial analysis based on the Frobenius method. The indicial exponents are 0, 1, 3 and 4, but Keiller neglected the exponents 0 and 1, thereby losing the leading-order behaviour of the stresses. Furthermore, no attempt was made to resolve the structure at the singular point. Sureshkumar & Beris (1995*b*) performed a somewhat heuristic analysis of the spectrum, hypothesizing that the stress fields contain delta-function singularities. As they note, their proposed stresses do not satisfy the momentum balance, and in fact the exact analysis presented below shows that no delta functions are present in the solution.

We begin the solution of (A 2) by writing it as

$$L_1 L_2 \hat{v}_r = 0,$$

https://doi.org/10.1017/S0022112098008611 Published online by Cambridge University Press

which can be rewritten

$$L_1 w = 0, \tag{A 4}$$

$$L_2 \hat{v}_r = w. \tag{A 5}$$

The substitution $w = \varrho f(\varrho)$ leads to the general solution for w:

$$w(\varrho) = k_3 \varrho \cosh(\alpha\varrho) + k_4 \varrho \sinh(\alpha\varrho), \tag{A 6}$$

where k_3 and k_4 are arbitrary constants. The general solution to $L_2\hat{v}_r = w$ is found to be

$$\begin{aligned}\hat{v}_r(\varrho) = {} & k_1 \exp\left(-\alpha\,\varrho\left[-\mathrm{i}\,We_z + \left(1 + We_z^2\right)^{1/2}\right]\right) \\ & + k_2 \exp\left(\alpha\,\varrho\left[\mathrm{i}\,We_z + \left(1 + We_z^2\right)^{1/2}\right]\right) \\ & + k_3 \frac{-(-\mathrm{i} + \alpha\, We_z\, \varrho)\,(We_z\, \cosh(\alpha\,\varrho) - \mathrm{i}\, \sinh(\alpha\,\varrho))}{2\,\alpha^3\, {We_z}^2\,\left(1 + {We_z}^2\right)} \\ & + k_4 \frac{-(-\mathrm{i} + \alpha\, We_z\, \varrho)\,(-\mathrm{i}\, \cosh(\alpha\,\varrho) + We_z\, \sinh(\alpha\,\varrho))}{2\,\alpha^3\, {We_z}^2\,\left(1 + {We_z}^2\right)},\end{aligned} \tag{A 7}$$

where k_1 and k_2 are new arbitrary constants.

At the singular point, the solution need not be analytic. In particular, note that the third-derivative term in (A2) is multiplied by ϱ and the fourth by ϱ^2. Now, if $\hat{v}_r$ is a C^1 function, then $\hat{v}_r''' \sim \delta(\varrho)$ and $\hat{v}_r'''' \sim \delta'(\varrho)$, and the third- and fourth-derivative terms look like $\varrho\delta(\varrho)$ and $\varrho^2\delta'(\varrho)$, which both vanish (Greenberg 1978). Therefore, the arbitrary 'constants' k_1–k_4 can take on different values on the two sides of the singular point, as long as the solutions and first derivatives on the two sides match at $\varrho = 0$ (and the boundary conditions are satisfied). The resulting solution will satisfy the equation in the whole domain, including the singular point. In addition, the solution will actually be C^2 even if only $\hat{v}_r(0)$ and $\hat{v}_r'(0)$ are imposed, because, since the third- and fourth-derivative terms vanish at $\varrho = 0$, the resulting second-order equation uniquely determines $\hat{v}_r''(0)$, given $\hat{v}_r(0)$ and $\hat{v}_r'(0)$. For comparison, the continuous spectrum of the stability problem for inviscid plane shear flow corresponds to C^0 functions (Case 1960). Both $\hat{v}_r(0)$ and $\hat{v}_r'(0)$ can be chosen arbitrarily, so each eigenvalue in the continuous spectrum is degenerate, having two linearly independent eigenfunctions. Finally, since both $\hat{v}_r$ and $\hat{v}_r'$ cannot vanish at $\varrho = 0$ (otherwise the trivial solution is obtained), (A 3) show that each of the exact stresses has a non-integrable singularity: $\hat{\tau}_{rr} \propto \varrho^{-1}, \hat{\tau}_{rz} \propto \varrho^{-2}, \hat{\tau}_{zz} \propto \varrho^{-3}$.

Figure 17 shows the two eigenfunctions (plotted against the original gap coordinate ρ) for $\alpha = 1, We_z = 10, \rho_0 = 0.8$, constructed by setting $\hat{v}_r(0) = 1, \hat{v}_r'(0) = 0$ for the first eigenfunction and $\hat{v}_r(0) = 0, \hat{v}_r'(0) = 1$ for the second. Table 3 gives the values of the coefficients in (A 7), where k_{il} and k_{ir} denote the values of k_i when $\varrho \leqslant 0$ and $\varrho > 0$, respectively.

Given the nature of the exact solution for these eigenfunctions, the numerical observations can be put into perspective. The pairing of modes on figure 16, one below each point on the exact spectrum and one above, arises from the twofold multiplicity of the exact eigenvalues. The slow convergence as N increases reflects the C^2 continuity; the error in Chebyshev approximation of a C^2 function is only $o(N^{-2})$ (Gottlieb & Orszag 1977). Nevertheless, the numerically observed velocities are smooth, reflecting the absence of any blowup in the exact velocities. The exact stresses, in contrast, are non-integrable, so no conventional numerical approach can

https://doi.org/10.1017/S0022112098008611 Published online by Cambridge University Press

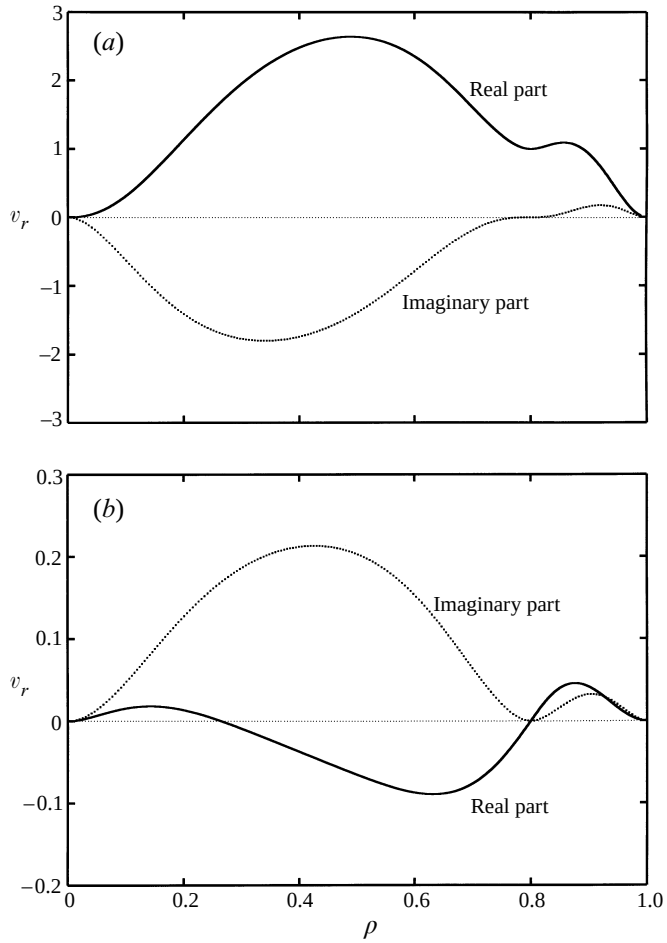


FIGURE 17. Eigenfunctions for the modes in the continuous spectrum, $\alpha = 1$, $We_z = 10$, $\rho_0 = 0.8$: (*a*) mode 1, satisfying $\hat{v}_r(\rho = 0.8) = 1$, $\hat{v}_r'(\rho = 0.8) = 0$; (*b*) mode 2, satisfying $\hat{v}_r(\rho = 0.8) = 0$, $\hat{v}_r'(\rho = 0.8) = 1$.

be expected to yield accurate approximations. The Chebyshev approximations to the stress fields are jagged, varying sharply at the grid scale near the singular point (cf. Sureshkumar & Beris 1995*b*). Furthermore, we have observed that the numerical modes exhibit the relation $||\hat{\tau}_{zz}|| \gg ||\hat{\tau}_{rz}|| \gg ||\hat{\tau}_{rr}||$, consistent with the exact singularity strengths.

For inertialess plane Poiseuille (PP) flow of the UCM fluid, no complete analytical description of the discrete spectrum exists, and the numerical analysis also remains incomplete, although no evidence has been found for instability. The first reliable computation of eigenvalues for this flow was performed by Ho & Denn (1977). Like the problem for Couette flow, the equation can be reduced to a fourth-order problem in the stream function; Ho & Denn used a shooting method to solve this form of the problem. They found four discrete eigenvalues, but did not describe the structure of the corresponding eigenfunctions. They also found a number of spurious eigenvalues. Sureshkumar & Beris (1995*b*), using a Chebyshev collocation method and a primitive variable formulation, computed the entire spectrum of the discretized problem. As in the Couette problem, there is a continuous spectrum, defined by

https://doi.org/10.1017/S0022112098008611 Published online by Cambridge University Press

Coefficient	Mode 1	Mode 2
k_{1l}	$-1.637\,43 \times 10^{-4} + \mathrm{i}3.634\,02 \times 10^{-4}$	$-9.885\,88 \times 10^{-6} - \mathrm{i}2.630\,92 \times 10^{-5}$
k_{2l}	$-0.173\,397 - \mathrm{i}1.1899$	$0.117\,868 + \mathrm{i}1.116\,38 \times 10^{-3}$
k_{3l}	$2727.27 - \mathrm{i}1954.72$	$-39.1109 + \mathrm{i}233.419$
k_{4l}	$4158.72 - \mathrm{i}3244.05$	$-46.5394 + \mathrm{i}369.09$
k_{1r}	$-1.078\,67 + \mathrm{i}3.881\,92$	$-0.283\,257 + \mathrm{i}0.106\,14$
k_{2r}	$-0.706\,126 + \mathrm{i}0.148\,871$	$-0.045\,218\,9 - \mathrm{i}0.021\,350\,3$
k_{3r}	$-8810.39 - \mathrm{i}66.2721$	$-448.03 - \mathrm{i}400.7$
k_{4r}	$55\,590.3 + \mathrm{i}6681.97$	$2628.22 + \mathrm{i}2767.55$

TABLE 3. Values of the coefficients of (A 7) for the modes in the continuous spectrum at $\alpha = 1, We_z = 10, \rho_0 = 0.8$. Mode 1 satisfies $\hat{v}_r(\rho = 0.8) = 1, \hat{v}_r'(\rho = 0.8) = 0$; mode 2 satisfies $\hat{v}_r(\rho = 0.8) = 0, \hat{v}_r'(\rho = 0.8) = 1$.

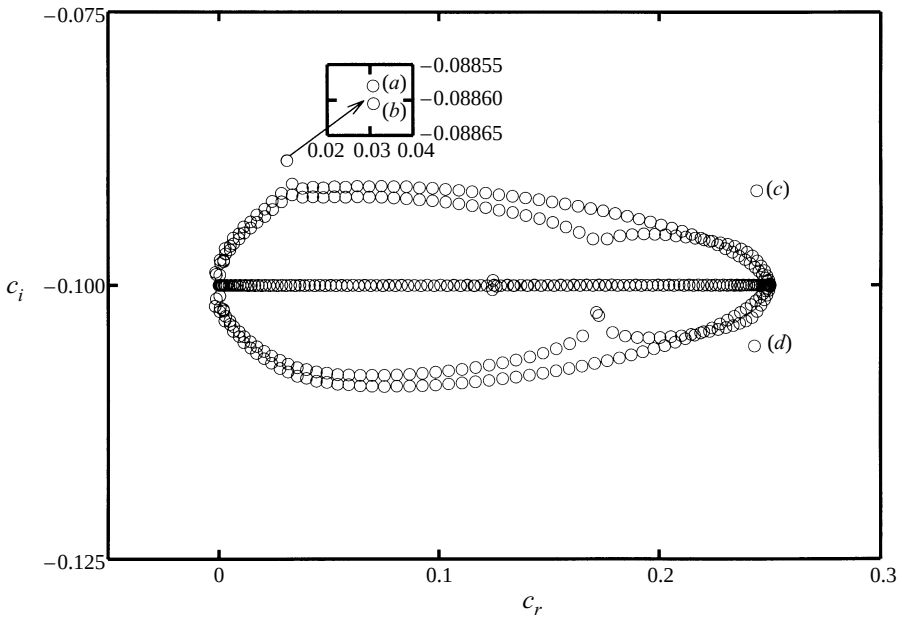


FIGURE 18. Spectrum of PP flow, $We_z = 1$, $\alpha = 10$, $N = 128$. This spectrum was obtained with the code used in the main text, with Wp set to 1×10^{-8} and the spectrum rescaled by We_z/Wp.

the strip $\{(1 - \rho_0)\rho_0 - \mathrm{i}/(\alpha We_z)\ \forall \rho_0 \in [0, 1]\}$, and as for numerical solution of the Couette case, Sureshkumar & Beris (1995*b*) found this strip to be approximated by a rough oval of eigenvalues. This is to be expected, as the C^2 continuity of $\hat{v}_r$, and the resulting singular stresses, carry over exactly to this case, except for the eigenvalue corresponding to a singularity at the midline (because there the velocity is locally quadratic rather than linear). They interpret their results as indicating that the spectrum of the numerical problem has six modes that are not approximations of elements of the continuous spectrum, and that four of these are spurious. Nevertheless, all six of these eigenvalues are insensitive to grid refinement. The results we present below support the view that Poiseuille flow has a family of at least four discrete eigenvalues, two of which are absent from the Couette problem.

We begin the present analysis of Poiseuille flow by presenting the numerically

https://doi.org/10.1017/S0022112098008611 Published online by Cambridge University Press

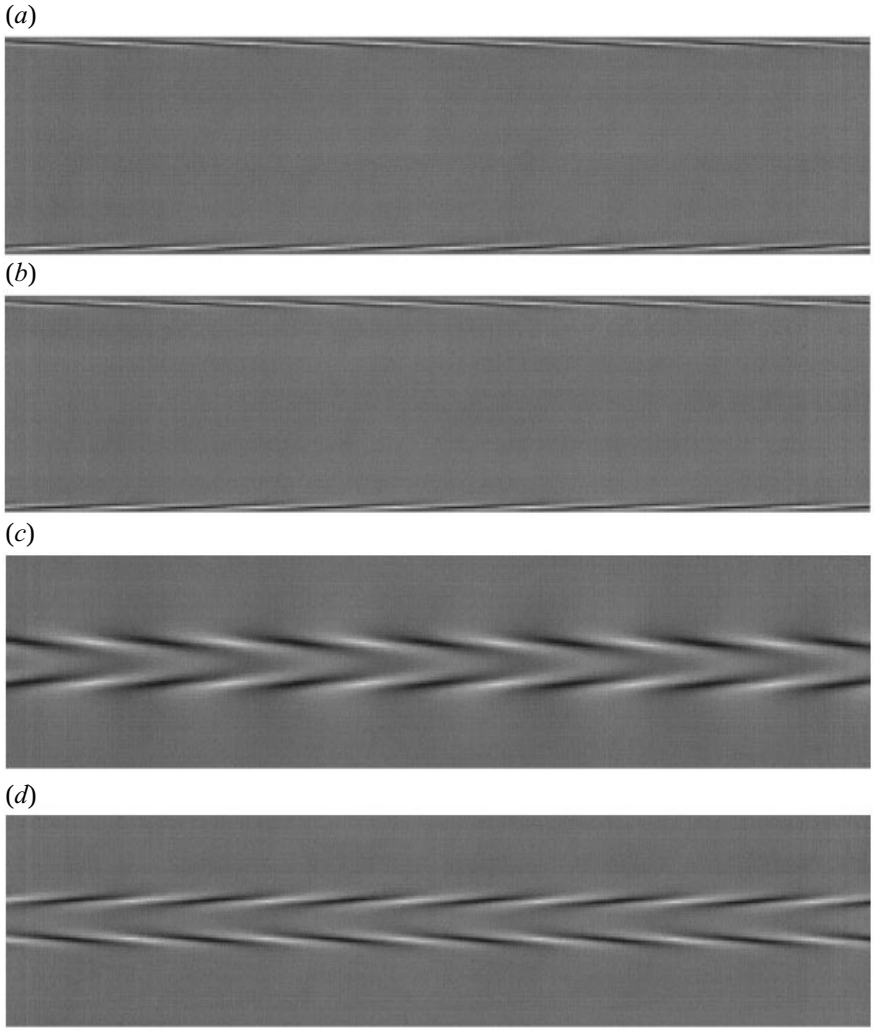


FIGURE 19. Snapshots of the disturbances (eigenfunctions) corresponding to eigenvalues (*a*)–(*d*) of the spectrum of PP flow, $We_z = 1$, $\alpha = 10$, $N = 128$ (figure 18). The disturbances are travelling waves that decay in time.

determined spectrum at $\alpha = 10, We_z = 1, N = 128$, figure 18. There are four obvious discrete eigenvalues, labelled (*a*)–(*d*), and an approximate continuous spectrum. There may be other discrete eigenvalues that cannot be resolved due to their proximity to the continuous spectrum. The four discrete eigenvalues are insensitive to further mesh refinement; there is no *a priori* reason to assume that they are not accurate approximations to the true continuous problem. The $\tilde{\tau}_{zz}$-components of the travelling wave disturbances corresponding to these discrete modes are shown in figure 19. Eigenvalues (*a*) and (*b*) are nearly identical to one another, and also nearly identical to the Gorodsov–Leonov eigenvalue for PC flow corresponding to the same wavenumber and Weissenberg number. Furthermore, the eigenvectors of modes (*a*) and (*b*) are strongly localized near the channel boundaries; one is even, the other odd across the channel midplane. We can understand these observations by noting that, near the channel boundaries, the flow looks locally like Couette flow, so that

https://doi.org/10.1017/S0022112098008611 Published online by Cambridge University Press

at high wavenumbers, eigenvalues should exist that have a structure like that of the Gorodtsov–Leonov eigenvalues. It is straightforward to show that by considering large-wavenumber disturbances (cf. Black & Graham 1996), a Gorodtsov–Leonov problem is recovered at leading order for fluctuations localized near each wall. As $\alpha \to \infty$, the strong localization implies that fluctuations near either wall should be decoupled from fluctuations at the other wall. The presence of a pair of nearly identical eigenvalues, having even and odd eigenvectors, allows this decoupling to be realized; any relative phase of the disturbances near the two boundaries can occur.

No corresponding asymptotic analysis has yet been performed to prove that eigenvalues (*c*) and (*d*) belong to the true spectrum of Poiseuille flow. Nevertheless, in addition to their insensitivity to grid resolution (for large N), another fact supports the contention that they are true eigenvalues. In the main text it is shown that one of the eigenvalues leading to the instability of CC flow, which is surely not spurious, evolves smoothly into mode (*c*) as parameters change. The relation of mode (*d*) to the spectrum of CC flow has not been determined, but its spatial structure is smooth and similar to that of mode (*c*), so no grounds exist for supposing that it is not a true eigenvalue of the PP spectrum. This pair of eigenvalues evidently comprises a family of modes that is distinct from the shear-dominated Gorodtsov–Leonov modes. The Gorodtsov–Leonov modes are essentially boundary layer modes at large wavenumber; in contrast, the other pair of modes can be thought of as *internal layer* perturbations. The results of the main text show that both families of modes can lead to instabilities in shear flows that are more complicated than the CC, PP and PC limits.

Appendix B. The governing equations in the narrow gap limit

This Appendix contains the formulas for the steady-state velocities and stresses in CCAC and CCAP flows, and the linear operator $\boldsymbol{L}$ of the generalized eigenvalue problem that determines their linear stability, to leading order in ϵ and under the assumptions and scalings described in the main text. When $We_z = 0, \tilde{n} = 0$, this formulation reduces to that of LSM.

B.1. *Base states*

To leading order, the steady-state velocities and polymer stresses for CCAC flow of an Oldroyd-B fluid are

$$\bar{v}_r = 0, \quad \bar{v}_\theta = (1-\rho), \quad \bar{v}_z = \frac{We_z\,(1-\rho)\,\epsilon^{1/2}}{Wp}, \tag{B 1}$$

$$\bar{\tau}_{rr} = 0, \quad \bar{\tau}_{r\theta} = -\frac{Wp}{(S+1)\,\epsilon^{1/2}}, \quad \bar{\tau}_{rz} = -\frac{We_z}{S+1}, \tag{B 2}$$

$$\bar{\tau}_{\theta\theta} = \frac{2\,Wp^2}{(S+1)\,\epsilon}, \quad \bar{\tau}_{\theta z} = \frac{2\,We_z\,Wp}{(S+1)\,\epsilon^{1/2}}, \quad \bar{\tau}_{zz} = \frac{2\,We_z^2}{S+1}. \tag{B 3}$$

For CCAP flow, the steady state is

$$\bar{v}_r = 0, \quad \bar{v}_\theta = (1-\rho), \quad \bar{v}_z = \frac{We_z\,(1-\rho)\,\rho\,\epsilon^{1/2}}{Wp}, \tag{B 4}$$

$$\bar{\tau}_{rr} = 0, \quad \bar{\tau}_{r\theta} = -\frac{Wp}{\epsilon^{1/2}}, \quad \bar{\tau}_{rz} = We_z\,(1-2\,\rho)\,/\,(S+1), \tag{B 5}$$

$$\bar{\tau}_{\theta\theta} = \frac{2\,Wp^2}{(S+1)\,\epsilon}, \quad \bar{\tau}_{\theta z} = -\frac{We_z\,Wp\,(2-4\,\rho)}{(S+1)\,\epsilon^{1/2}}, \quad \bar{\tau}_{zz} = \frac{We_z{}^2\,(2-4\,\rho)^2}{2\,(S+1)}. \tag{B 6}$$

https://doi.org/10.1017/S0022112098008611 Published online by Cambridge University Press

B.2. *Linear stability problem*

Here are listed the non-zero elements of the operator $\boldsymbol{L}_{\alpha,\tilde{n}}$ for the linear stability problem, (2.6) for the CCAC and CCAP flows. The first six rows of $\boldsymbol{L}_{\alpha,\tilde{n}}$ correspond to the constitutive equation, the seventh and eighth to the r- and θ-vorticity equations and the ninth to the continuity equation. Setting $\tilde{n}$ to zero gives the operator $\boldsymbol{L}_{\alpha}$ used in the weakly nonlinear analysis.

B.2.1. *CCAC flow*

$$L_{11} = -\mathrm{i}\alpha\frac{We_z}{Wp}(1-\rho) - \mathrm{i}\tilde{n}(1-\rho) - \frac{1}{Wp}, \quad L_{17} = (2\mathrm{D} - 2\mathrm{i}\alpha We_z - 2\tilde{n}Wp)/(S+1),$$

$$L_{21} = -1, \quad L_{22} = L_{11}, \quad L_{27} = Wp(2\mathrm{i}\alpha We_z + 2\mathrm{i}\tilde{n}Wp - \mathrm{D})/(S+1),$$
$$L_{28} = (-\mathrm{i}\alpha We_z - \mathrm{i}\tilde{n}Wp + \mathrm{D})/(S+1),$$

$$L_{31} = -\frac{We_z}{Wp}, \quad L_{33} = L_{11}, \quad L_{37} = \left(\mathrm{i}\alpha\left(1+2We_z^2\right) + 2\tilde{n}We_z Wp - We_z\mathrm{D}\right)/(S+1),$$
$$L_{39} = (-\mathrm{i}\alpha We_z - \mathrm{i}\tilde{n}Wp + \mathrm{D})/(S+1),$$

$$L_{42} = -2, \quad L_{44} = L_{11}, \quad L_{48} = Wp\,(4\mathrm{i}\alpha We_z + 4\mathrm{i}\tilde{n}Wp - 2\mathrm{D})/(S+1),$$

$$L_{52} = -\frac{We_z}{Wp}, \quad L_{53} = -1, \quad L_{55} = L_{11},$$
$$L_{58} = \left(\mathrm{i}\alpha\left(1+2We_z^2\right) + 2\mathrm{i}\tilde{n}We_z Wp - We_z\mathrm{D}\right)/(S+1),$$
$$L_{59} = \left(2\mathrm{i}\alpha We_z Wp + 2\mathrm{i}\tilde{n}Wp^2 - Wp\mathrm{D}\right)/(S+1),$$

$$L_{63} = -2\frac{We_z}{Wp}, \quad L_{66} = L_{11}, \quad L_{69} = \left(2\mathrm{i}\alpha\left(1+2We_z^2\right) + 4\mathrm{i}\tilde{n}We_z Wp - 2We_z\mathrm{D}\right)/(S+1),$$

$$L_{72} = \mathrm{D}, \quad L_{74} = \mathrm{i}\tilde{n}, \quad L_{75} = \mathrm{i}\alpha, \quad L_{78} = SWp\left(-\alpha^2 + \mathrm{D}^2\right)/(S+1),$$

$$L_{81} = \mathrm{i}\alpha\mathrm{D}, \quad L_{82} = -\tilde{n}\alpha, \quad L_{83} = -\alpha^2 - \mathrm{D}^2, \quad L_{84} = -\mathrm{i}\alpha, \quad L_{85} = -\mathrm{i}\tilde{n}\mathrm{D},$$
$$L_{86} = -\mathrm{i}\alpha\mathrm{D}, \quad L_{87} = \mathrm{i}\alpha SWp\left(-\alpha^2 + \mathrm{D}^2\right)/(S+1), \quad L_{89} = SWp\left(\alpha^2\mathrm{D} - \mathrm{D}^3\right)/(S+1),$$

$$L_{97} = D, \quad L_{98} = \mathrm{i}\tilde{n}, \quad L_{99} = \mathrm{i}\alpha.$$

B.2.2. *CCAP flow*

$$L_{11} = -\mathrm{i}\alpha\frac{We_z}{Wp}(1-\rho)\rho - \mathrm{i}\tilde{n}(1-\rho) - \frac{1}{Wp},$$
$$L_{17} = (2\mathrm{D} - 2\mathrm{i}\alpha We_z(2\rho-1) - 2\tilde{n}Wp)/(S+1),$$

$$L_{21} = -1, \quad L_{22} = L_{11}, \quad L_{27} = Wp(2\mathrm{i}\alpha We_z(2\rho-1) + 2\mathrm{i}\tilde{n}Wp - D)/(S+1),$$
$$L_{28} = (-\mathrm{i}\alpha We_z(2\rho-1) - \mathrm{i}\tilde{n}Wp + \mathrm{D})/(S+1),$$

$$L_{31} = -\frac{We_z(2\rho-1)}{Wp}, \quad L_{33} = L_{11},$$
$$L_{37} = \left(\mathrm{i}\alpha\left(1+2We_z^2(2\rho-1)^2\right) + 2We_z + 2\tilde{n}We_z(2\rho-1)Wp - We_z(2\rho-1)\mathrm{D}\right)/(S+1),$$
$$L_{39} = (-\mathrm{i}\alpha We_z(2\rho-1) - \mathrm{i}\tilde{n}Wp + \mathrm{D})/(S+1),$$

https://doi.org/10.1017/S0022112098008611 Published online by Cambridge University Press

$$L_{42} = -2, \quad L_{44} = L_{11}, \quad L_{48} = Wp\,(4\mathrm{i}\alpha We_z(2\rho - 1) + 4\mathrm{i}\tilde{n}Wp - 2\mathrm{D})\,/(S+1),$$

$$L_{52} = -\frac{We_z(2\rho-1)}{Wp}, \quad L_{53} = -1, \quad L_{55} = L_{11}, \quad L_{57} = -4We_z Wp/(S+1),$$

$$L_{58} = \left(\mathrm{i}\alpha\left(1 + 2We_z^2(2\rho-1)^2\right) + 2\mathrm{i}\tilde{n}We_z(2\rho-1)Wp - We_z(2\rho-1)\mathrm{D}\right)/(S+1),$$

$$L_{59} = \left(2\mathrm{i}\alpha We_z(2\rho-1)Wp + 2\mathrm{i}\tilde{n}Wp^2 - Wp\mathrm{D}\right)/(S+1),$$

$$L_{63} = -2\frac{We_z(2\rho-1)}{Wp}, \quad L_{66} = L_{11}, \quad L_{67} = 8We_z^2(2\rho-1)/(S+1),$$

$$L_{69} = \left(2\mathrm{i}\alpha\left(1 + 2We_z^2(2\rho-1)^2\right) + 4\mathrm{i}\tilde{n}We_z(2\rho-1)Wp - 2We_z(2\rho-1)\mathrm{D}\right)/(S+1).$$

The vorticity and continuity equations are unchanged from the CCAC case.

REFERENCES

Avgousti, M. & Beris, A. N. 1993*a* Non-axisymmetric modes in the viscoelastic Taylor–Couette flow. *J. Non-Newtonian Fluid Mech.* **50**, 225–252.

Avgousti, M. & Beris, A. N. 1993*b* Viscoelastic Taylor–Couette flow: bifurcation analysis in the presence of symmetries. *Proc. R. Soc. Lond.* A **443**, 17–38.

Avgousti, M., Liu, B. & Beris, A. N. 1993 Spectral methods for the viscoelastic time-dependent flow equations with applications to Taylor–Couette flow. *Intl J. Numer. Meth. Fluids* **17**, 49–74.

Azaiez, J. & Homsy, G. M. 1994 Linear stability of free shear flow of viscoelastic liquids. *J. Fluid Mech.* **268**, 37–69.

Baumert, B. M. & Muller, S. J. 1995 Flow visualization of the elastic Taylor–Couette instability in Boger fluids. *Rheol. Acta* **34**, 147–159.

Beris, A. N., Avgousti, M. & Souvaliotis, A. 1992 Spectral calculations of viscoelastic flows: evaluation of the Giesekus constitutive equation in model flow problems. *J. Non-Newtonian Fluid Mech.* **44**, 197–228.

Black, W. B. & Graham, M. D. 1996 Wall-slip and polymer-melt flow instability. *Phys. Rev. Lett.* **77**, 956–959.

Canuto, C., Hussaini, M. Y., Quarteroni, A. & Zang, T. A. 1988 *Spectral Methods in Fluid Dynamics.* Springer.

Case, K. M. 1960 Stability of inviscid plane Couette flow. *Phys. Fluids* **3**, 143–148.

Chandrasekhar, S. 1981 *Hydrodynamic and Hydromagnetic Stability.* Dover.

Chossat, P. & Iooss, G. 1994 *The Couette-Taylor Problem.* Springer.

Datta, S. K. 1964 Note on the stability of an elasticoviscous liquid in Couette flow. *Phys. Fluids* **7**, 1915–1919.

Denn, M. M. & Roisman, J. J. 1969 Rotational stability and measurement of normal stress functions in dilute polymer solutions. *AIChE J.* **15**, 454–459.

Drazin, P. G. & Reid, W. H. 1981 *Hydrodynamic Stability.* Cambridge University Press.

Feinberg, M. R. & Schowalter, W. R. 1969*a* Conditions for the stability of cylindrical Couette flow of certain viscoelastic liquids. In *Proc. Fifth Intl Congress on Rheology* (ed. S. Onogi). University of Tokyo Press.

Feinberg, M. R. & Schowalter, W. R. 1969*b* Sufficient conditions for stability of fluid motions constitutively described by the infinitesimal theory of viscoelasticity. *I& EC Fundam.* **8**, 332–338.

Garbow, B. S. 1978 Algorithm 535: the QZ algorithm to solve the generalized eigenvalue problem for complex matrices. *ACM Trans. Math. Software* **4**, 404–410.

Giesekus, H. 1971 *Progress in Heat and Mass Transfer*, vol. 5, pp. 187–209. Pergamon.

Ginn, R. F. & Denn, M. M. 1969 Rotational stability in viscoelastic fluids: Theory. *AIChE J.* **15**, 450–454.

Golubitsky, M., Schaeffer, D. G. & Stewart, I. 1985 *Singularities and Groups in Bifurcation Theory*, Vol. 2. Springer.

https://doi.org/10.1017/S0022112098008611 Published online by Cambridge University Press

Gorodtsov, V. A. & Leonov, A. I. 1967 On a linear instability of a plane parallel Couette flow of viscoelastic fluid. *J. Appl. Math. Mech.* **31**, 310–319.

Gottlieb, D. & Orszag, S. A. 1977 *Numerical Analysis of Spectral Methods.* SIAM.

Graham, M. D. & Steen, P. H. 1991 Structure and mechanism of oscillatory convection in a cube of fluid-saturated porous material heated from below. *J. Fluid. Mech.* **232**, 591–609.

Greenberg, M. D. 1978 *Foundations of Applied Mathematics.* Prentice-Hall.

Ho, T. C. & Denn, M. M. 1977 Stability of plane Poiseuille flow in a highly elastic liquid. *J. Non-Newtonian Fluid Mech.* **3**, 179–195.

Iooss, G. & Joseph, D. D. 1990 *Elementary Bifurcation and Stability Theory*, 2nd edn. Springer.

Joo, Y. L. & Shaqfeh, E. S. G. 1992 A purely elastic instability in Dean and Taylor-Dean flow. *Phys. Fluids* A **4**, 524–543.

Joo, Y. L. & Shaqfeh, E. S. G. 1994 Observations of purely elastic instabilities in the Taylor–Dean flow of a Boger fluid. *J. Fluid Mech.* **262**, 27–73.

Keiller, R. A. 1992 Numerical instability of time-dependent flows. *J. Non-Newtonian Fluid Mech.* **43**, 229–246.

Larson, R. G., Shaqfeh, E. S. G. & Muller, S. J. 1990 A purely elastic instability in Taylor–Couette flow. *J. Fluid Mech.* **218**, 573–600 (referred to herein as LSM).

Marques, F. & Lopez, J. M. 1997 Taylor-Couette flow with axial oscillations of the inner cylinder: Floquet analysis of the basic flow. *J. Fluid Mech.* **348**, 158–175.

Muller, S. J., Shaqfeh, E. S. G. & Larson, R. G. 1993 Experimental studies of the onset of oscillatory instability in viscoelastic Taylor–Couette flow. *J. Non-Newtonian Fluid Mech.* **46**, 315–330.

Northey, P. J., Armstrong, R. C. & Brown, R. A. 1992 Finite-amplitude time-periodic states in viscoelastic Taylor–Couette flow described by the UCM model. *J. Non-Newtonian Fluid Mech.* **42**, 117–139.

Pakdel, P. & McKinley, G. H. 1996 Elastic instability and curved streamlines. *Phys. Rev. Lett.* **77**, 2459–2462.

Rallison, J. M. & Hinch, E. J. 1995 Instability of a high-speed submerged jet. *J. Fluid Mech.* **288**, 311–324.

Renardy, M. 1992 A rigorous stability proof for plane Couette flow of an upper convected Maxwell fluid at zero Reynolds number. *Eur. J. Mech.* B/*Fluids* **11**, 511–516.

Renardy, M. 1997 High Weissenberg number boundary layers for the upper convected Maxwell fluid. *J. Non-Newtonian Fluid Mech.* **68**, 125–132.

Renardy, M. & Renardy, Y. 1986 Linear stability of plane Couette flow of an upper convected Maxwell fluid. *J. Non-Newtonian Fluid Mech.* **22**, 23–33.

Renardy, M., Renardy, Y., Sureshkumar, R. & Beris, A. N. 1996 Hopf-Hopf and steady-Hopf mode interactions in Taylor–Couette flow of an upper convected Maxwell liquid. *J. Non-Newtonian Fluid Mech.* **63**, 1–31.

Rubin, H. & Elata, C. 1966 Stability of Couette flow of dilute polymer solutions. *Phys. Fluids* **9**, 1929–1933.

Serrin, J. 1959 On the stability of viscous fluid motions. *Arch. Rat. Mech. Anal.* **3**, 1–13.

Shaqfeh, E. S. G. 1996 Purely elastic instabilities in viscometric flows. *Ann. Rev. Fluid Mech.* **28**, 129–185.

Shaqfeh, E. S. G., Muller, S. J. & Larson, R. G. 1992 The effects of gap width and dilute solution properties on the viscoelastic Taylor–Couette instability. *J. Fluid Mech.* **235**, 285–317.

Steen, P. H. & Aidun, C. K. 1988 Time-periodic convection in porous media: transition mechanism. *J. Fluid Mech.* **136**, 219–241.

Sun, Z.-S. & Denn, M. M. 1972 Stability of rotational Couette flow of polymer solutions. *AIChE J.* **18**, 1010–1015.

Sureshkumar, R. & Beris, A. N. 1995*a* Effect of artificial stress diffusivity on the stability of numerical calculations and the flow dynamics of time-dependent viscoelastic flows. *J. Non-Newtonian Fluid Mech.* **60**, 53–80.

Sureshkumar, R. & Beris, A. N. 1995*b* Linear stability analysis of viscoelastic Poiseuille flow using an Arnoldi-based orthogonalization algorithm. *J. Non-Newtonian Fluid Mech.* **56**, 151–182.

Sureshkumar, R., Beris, A. N. & Avgousti, M. 1994 Non-axisymmetric subcritical bifurcations in viscoelastic Taylor–Couette flow. *Proc. R. Soc. Lond.* A **447**, 135–153.

https://doi.org/10.1017/S0022112098008611 Published online by Cambridge University Press

Swinney, H. L. & Gollub, J. P. (Eds.) 1985 *Hydrodynamic Instabilities and the Transition to Turbulence*. Springer.

Thomas, R. H. & Walters, K. 1964 The stability of elastico-viscous flow between rotating cylinders. Part 1. *J. Fluid Mech.* **18**, 33–43.

Tlapa, G. & Bernstein, B. 1970 Stability of a relaxation-type viscoelastic fluid with slight elasticity. *Phys. Fluids* **13**, 565–568.

Weisberg, A. Y., Kevrekidis, I. G. & Smits, A. J. 1997 Delaying transition in Taylor-Couette flow with axial motion of the inner cylinder. *J. Fluid Mech.* **348**, 141–152.

https://doi.org/10.1017/S0022112098008611 Published online by Cambridge University Press